A resistive-capacitive model of pile heat exchangers with an application to thermal response tests interpretation

Author 1:
Given Name: Charles
Family name: Maragna
Affiliation: BRGM
E-mail: c.maragna@brgm.fr
Postal address: BRGM, 3 Avenue Claude Guillemin, BP 36009 - 45060 Orléans cedex 2, France

Author 2:
Given name: Fleur
Family Name: Loveridge
Affiliation: University of Leeds
E-mail: f.a.loveridge@leeds.ac.uk
Postal address: School of Civil Engineering, University of Leeds, Woodhouse Lane, Leeds. LS2 9JT

Contact author: Charles Maragna

Highlights

- A new finite cylindrical source model with adiabatic surface is developed.
- A new resistive-capacitive semi-analytical pile heat exchanger model is developed.
- The new model improves the assessment of pile thermal performance.
- Neglecting heat capacitance in the pile leads to an underestimation of performance.
- The new model is successfully used to interpret a thermal response test.

Abstract

Pile Heat Exchangers (PHE) are an attractive solution to reduce both costs and greenhouse gas emissions for new buildings. However, most state-or-the-art PHE thermal models overlook the heat capacitance of the pile concrete, which is known to be important in thermal analysis. A semi-analytical (SA) model accounting for the pile concrete inertia is developed and validated against a finite-element code. Analysis shows that accounting for PHE inertia always leads to higher performances compared to purely resistive models. Application of the model to interpretation of thermal response tests data allows estimates to be made of the minimum duration test required to obtain reliable values of ground and concrete conductivities.

Keywords

- Pile heat exchangers
- Thermal models
- Thermal response test
- Near-surface geothermal energy
- Ground source heat pumps

Graphical abstract

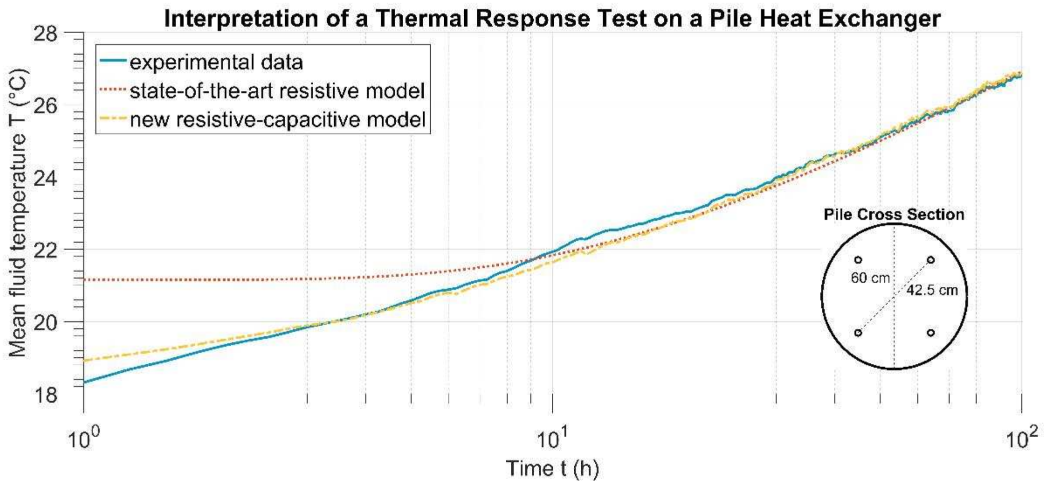

Nomenclature

Latin Letters		Subscripts	
a	thermal diffusivity ($m.s^{-2}$)	0	undisturbed conditions
$\mathcal{C}$	capacity of a node ($J.K^{-1}.m^{-1}$)	b	borehole wall
e	energy per meter of pile ($J.m^{-1}$)	c	concrete
$\dot{m}$	flow rate ($kg.s^{-1}$)	fl	heat-carrier fluid
r	radius	in	inlet
R	thermal resistance ($K.m.W^{-1}$)	m	ground
p	power per meter of pile ($W.m^{-1}$)	out	outlet
T	temperature (°C)	p	pipe
t	time (s)	∞	steady-state value
t*	normalized time (Fourier number)		
x, y	capacities locations in the RC circuit		
Greek letters		Superscripts	
ε	misfit (root mean square error)		
λ	thermal conductivity ($W.K^{-1}.m^{-1}$)	n	time step n
$[\Lambda]$	Conductance matrix ($W.K^{-1}.m^{-1}$)	*	normalized value
ρC_p	volume-specific heat capacity ($J.K^{-1}.m^{-3}$)	$\Phi 0$	adiabatic condition at the surface
		T0	imposed temperature at the surface
Acronyms			
GHE	Ground Heat Exchanger		
PHE	Pile Heat Exchanger		
FE	Finite Elements		
RC	Resistive-Capacitive		
ICS	Infinite Cylindrical Source		
ILS	Infinite Line Source		
SA	Semi-Analytical		
FLS	Finite Line Source		

Introduction

Ground-sourced heat pumps (GSHP) can significantly reduce CO_2 emissions associated with new buildings. However high investment cost is a limitation to the deployment of this technology. As a consequence in France the number of yearly installed GSHP collapsed from 15,500 to 3,200 between 2010 and 2014 [1] [2]. Cost-effective systems have to be found to reduce GSHP capital costs. Energy geostructures such as Pile Heat Exchangers (PHE) are one solution, since they couple the structural role of the geostructure with that of ground-sourced heat exchangers.

PHE are superficially similar to borehole heat exchangers (BHE), but although BHE sizing tools are available to engineers, including pre-sizing Excel sheets (AHSRAE), bespoke software (EED) and dynamics simulation tools (TRNSYS-DST, FEFLOW), there are few PHE sizing tools, with the commercial software PILESIM [3] being the main example.

This lack of design tools is partly due to the fact that thermal modelling of PHE is more complex than BHE. PHE radius can exceed 50 cm and, compared with BHE which have a typical radius of <10 cm. Accurate description of the heat storage in the pile concrete is therefore needed [4]. Furthermore, typical PHE depths are in the range 10-30 m, where 100-200 m deep BHE are typical. The aspect ratio (the ratio between the depth and the pile radius) is therefore much lower for PHE than for BHE. Consequently vertical heat transfers around a PHE play a significant role earlier than for BHE.

In addition to design, pile characterisation for determination of analysis input parameters, requires realistic models of the pile capacitance. Current methodologies for the interpretation of thermal response tests (TRT) overlook internal heat capacitance within the PHE. Therefore, reliable PHE sizing also requires the development of relevant methodologies for the implementation and interpretation of TRT.

This paper presents a new model of PHE. The paper starts with a brief description of the state of the art concerning PHE models (Section 1). Then the construction of the new semi-analytical models are discussed in Section 2. The model combines relevant step-responses (G-functions) accounting for PHE aspect ratio with resistive-capacitive circuits. The model is validated against a fully discretized finite-element model and its domain of validity and limitations are highlighted. The model's performance compared with existing approaches is then set out (Section 4). The model is finally used to analyse thermal response test (TRT) data (Section 4), and investigate the reliability of interpretation based on the TRT duration. Though much work is carried out considering the implication of operation of energy piles on the stresses and strains, the paper focuses on thermal models does not include any thermo-mechanical assessment. The aim of the article is to provide a fast and accessible algorithm for engineering practices in order to compute the PHE fluid temperature evolution, avoiding the use of complex, resource-consuming and expensive discretized numerical models.

1. Model State of the Art

Most PHE thermal models are either numerical, analytical or apply a combination of both these techniques. Fully discretised models tend to be more accurate, but at the expense of computational effort. Techniques may include finite element analysis (e.g. [5]) or finite difference analysis (e.g. [6], [7], [8]). Numerical simulation is also commonly used as a research tool, for example to investigation of pipe arrangements and thermal performance (e.g. [9], [10], [11], [12], [13], [14], [15], [16], [17]), but is rarely practical for routine applications.

The state of art focuses on analytical models as they are more suitable for routine use than fully discretised models. Analytical models can run over reasonable time frames, i.e. performing simulations over 30 years with hourly time step, without resorting to super computing. The functions produced by the analytical models are often referred to as "step-responses" or G-functions (after the early work on BHEs by Eskilson [18]). Step responses describe the evolution of the normalized temperature of the borehole or pile perimeter under a constant power applied by unit length p ($W.m^{-1}$). The evolution of the temperature change ΔT is then given by:

$$\Delta T = \frac{p}{\lambda_m} G(t^*) \tag{1}$$

Where G(t*) is the response function and t* is a dimensionless time factor (Fourier number) and λ_m the ground thermal conductivity ($W.K^{-1}.m^{-1}$). G-functions are usually configured so that the temperature computed is that at the borehole (or pile) wall.

Common G-functions consider that heat can only be transferred by conduction. Convection, i.e. heat transport by water flow, is usually overlooked. The simplest BHE G-function, the infinite line source (ILS) model, represents the borehole as an infinite line emitting a constant heat flux [19]. Further improvements of the geometrical representation include the finite line source (FLS) model [18] and the hollow infinite cylindrical source (HICS) [20] [21] and solid cylindrical heat source [22].

The ILS, FLS and HICS G-functions are often coupled with resistive-capacitive (RC) circuits dealing with the thermal transfer within the borehole itself. While early developments were purely resistive, overlooking the thermal inertia of the grouting material [23] [24] [25], recent works have focused on developing full resistive-capacitive circuits for single U-tube (equipped with 2 pipes) BHE [26] [27] [28] [29] [30] or double U-tube BHE (equipped with 4 pipes) [31] [32]. However, pile heat exchangers of large diameter equipped with 8 or 10 pipes are not unusual.

Recent research on developing G-functions dedicated to PHE have also focused on dealing with the thermal inertia of the concrete, as well as accommodating a greater number of pipes and reduced aspect ratio $H^* = H/r_b$. Due to the large number of parameters characterising the pile and the ground, it is difficult to find a universal G-function for PHE. Loveridge and Powrie set up a practical approach where they defined extreme PHE configurations, leading to lower and upper bounds of numerically computed PHE G-functions. Single-pile [4] and multi-pile configurations [33] are provided, along with additional step response functions to cover the pile inertia which are included via superposition.

Bozis et al. developed an analytical method to compute the G-function for a single pile equipped with multiple pipes and provided an analytical expression of G as a function of the number and location of the pipes within the borehole [34]. They produced easy-to-use graphs that may be used for engineering applications, though the methodology holds only if the properties of the pile concrete and surrounding ground are the same.

Li and Lai took a different approach, developing G-functions that dealt with the pile inertia explicitly [35]. They applied the infinite line-source theory in composite media accounting directly for the contrast in thermal properties of the concrete and the ground. The approach is elegant but requires derivation for every pipe arrangement. Hence it requires a database similar to that of Eskilson for routine implementation [18]. Analytical models of spiral coils PHE have been developed for homogenous ([36], [37]) or heterogeneous [38] ground conditions, some of them being able to distinguish ground and concrete properties [39].

Zarella et al. developed a model for PHE equipped with 6 pipes, which can be generalized to any number of pipe [40]. However, this model still requires a steady-state resistance, which can be calculated from numerical models or from analytical formulae available in literature. While finite difference or finite elements are often time-consuming, the accuracy of borehole thermal resistance calculation methods is still an open question [41].

The final option for pile analysis is the Duct Storage model [23] which underpins the software PILESIM [3]. The model superimposes three solutions, a steady state solution for within the ground heat exchanger, a local ILS, and a global interaction between the underground thermal store and the surrounding soil. While developed for boreholes, but later validated for piles, it is limited by both use of the ILS and a steady resistance within the pile.

We present both a new pile G-function and importantly a resistive-capacitive model for a PHE equipped with 4 pipes. This model requires material thermo-physical properties and PHE geometrical properties to compute the evolution of the fluid temperature. Contrarily to the Zarella model [40], no intermediate parameters must be calculated externally by the user, which results in a more straight-forward workflow.

2. Model Development

In the development of the new model, the following assumptions are made:

(i) Physical properties of the materials (underground water, soil matrix, PHE heat carrier fluid) do not depend upon temperature.
(ii) The initial, non-disturbed temperature T_0 is constant in the whole domain and remains constant far away from the pile heat exchanger.
(iii) Both the ground and the pile concrete are regarded as homogenous and impervious media.

The heat is transferred in the ground and in the pile by conduction. The partial derivative equation for energy conservation reads:

$$\left(\rho C_p\right)_i \frac{\partial T}{\partial t} = \lambda_i \, \Delta T \tag{2}$$

λ accounts for the thermal conductivity of materials (W.K^{-1}.m^{-1}) and (ρC_p) for the volumetric heat capacity (J.K^{-1}.m^{-3}). The subscripts i refers to the solid material – the ground media is subscripted m and the concrete subscripted c.

The dimensionless time factor t* (Fourier number) is introduced to characterize the ratio of diffused heat to stored heat:

$$t^* = \frac{\lambda_i}{\left(\rho C_p\right)_i {r_b}^2} t \tag{3}$$

Note that the normalization length is r_b, the pile radius. This leads to the heat equation under its normalized form:

$$\frac{\partial T^*}{\partial t^*} = \Delta^* T^* \tag{4}$$

2.1. Development of Hollow Finite Cylindrical Source (HFCS) G-functions

Finite line source, $G_{FLS}(t^*)$, and hollow infinite cylindrical source, $G_{HICS}(t^*)$, G-functions are not suitable for PHE modelling due to the short aspect ratio. However no hollow finite cylindrical source, $G_{HFCS}(t^*)$, has been developed so far. Furthermore, the “classical” FLS model assumes that a constant temperature T_0 equal to the mean temperature of the ground is imposed at the surface. However, this assumption does not seem realistic for PHE as they are located below buildings whose basement is insulated. Therefore an adiabatic condition at the surface was assumed while developing the HFCS model. The impact of the type of upper boundary condition (imposed temperature or insulation) was quantified with the FLS model. The “classical”, temperature-imposed FLS (denoted FLS^{T0}) subtracts a “mirror” term from a “source” term [42], while in the adiabatic version ($FLS^{\Phi 0}$) both terms are added:

$$\begin{aligned}
G_{FLS}{}^{T0}(t^*) &= \frac{1}{2\pi}\left[\left(-D_A + \int_{\beta}^{\sqrt{\beta^2+1}} \frac{erfc(\omega z)}{\sqrt{z^2-\beta^2}}dz\right) - \left(D_B + \int_{\sqrt{\beta^2+1}}^{\sqrt{\beta^2+4}} \frac{erfc(\omega z)}{\sqrt{z^2-\beta^2}}dz\right)\right]\\
G_{FLS}{}^{\Phi 0}(t^*) &= \frac{1}{2\pi}\left[\left(-D_A + \int_{\beta}^{\sqrt{\beta^2+1}} \frac{erfc(\omega z)}{\sqrt{z^2-\beta^2}}dz\right) + \left(D_B + \int_{\sqrt{\beta^2+1}}^{\sqrt{\beta^2+4}} \frac{erfc(\omega z)}{\sqrt{z^2-\beta^2}}dz\right)\right]\\
D_A &= \sqrt{\beta^2+1}\ \mathrm{erfc}\left(\omega\sqrt{\beta^2+1}\right) - \beta\,\mathrm{erfc}(\omega\,\beta)\\
&\quad - \frac{\left(\exp\left(-\omega^2(\beta^2+1)\right) - \exp(-\omega^2\beta^2)\right)}{\omega\sqrt{\pi}}\\
D_B &= \sqrt{\beta^2+1}\ \mathrm{erfc}\left(\omega\sqrt{\beta^2+1}\right) - \frac{1}{2}\left(\beta\,\mathrm{erfc}(\omega\,\beta) + \sqrt{\beta^2+4}\,\mathrm{erfc}\left(\omega\sqrt{\beta^2+4}\right)\right)\\
&\quad - \frac{\left(\exp\left(-\omega^2(\beta^2+1)\right) - \frac{1}{2}\left(\exp(-\omega^2\beta^2) + \exp\left(-\omega^2(\beta^2+4)\right)\right)\right)}{\omega\sqrt{\pi}}
\end{aligned} \tag{5}$$

$$\omega = \frac{H}{2\sqrt{a_m t}} = \frac{H^*}{2\sqrt{t^*}}$$
$$\beta = \frac{r_b}{H} = \frac{1}{H^*}$$

In eq. (5), H accounts for the ground heat exchanger depth (m), a_m the ground diffusivity ($m^2.s^{-1}$), t the time (s) and r_b the ground heat exchanger radius. Assuming an adiabatic condition leads to much higher values of the G-function than assuming a fixed temperature (Figure 1). Short boreholes lead to larger discrepancies.

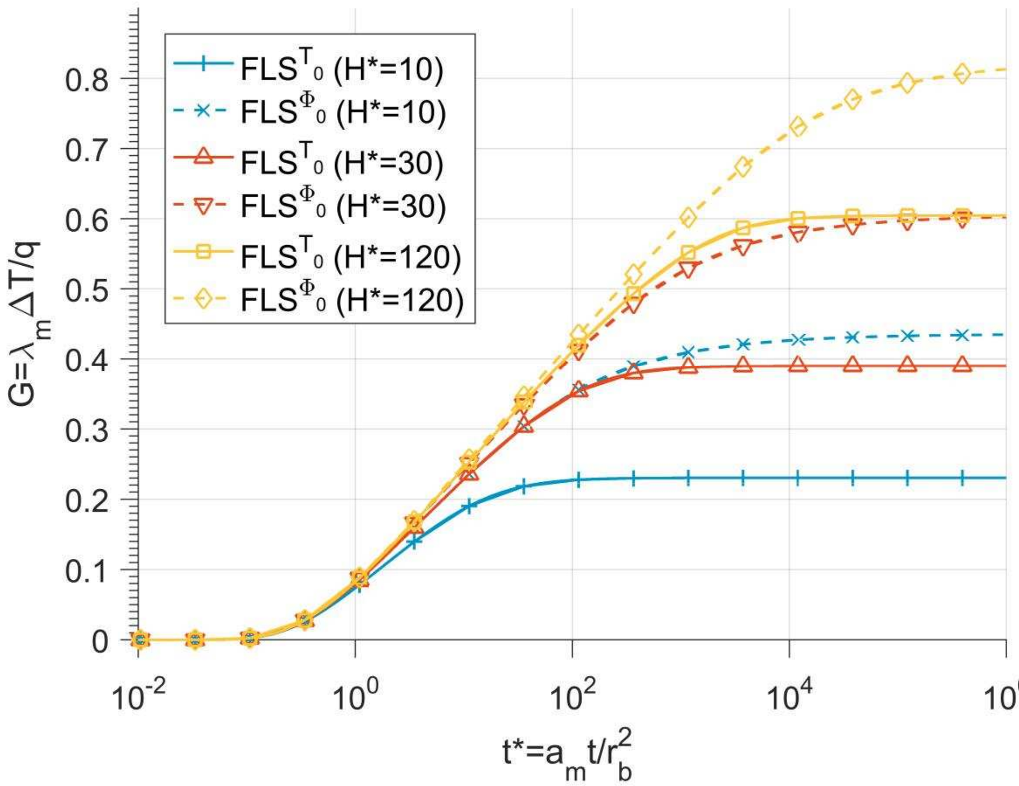

Figure 1: Comparison of the step responses G produced by the FLS model with 2 types of boundary conditions at the surface: either temperature imposed, the most common approach (denoted T_0), or adiabatic condition (denoted Φ_0)

This highlights that for short pile heat exchangers the G-function assuming a constant temperature at the ground surface can be up to approximately 25 % lower than the G-function assuming adiabatic conditions. Some research is still needed to better understand the influence of the top boundary on the G-function.

In the remaining parts of the paper we will evaluate finite models assuming an adiabatic condition at the top surface ($FLS^{\Phi 0}$ and $HFCS^{\Phi 0}$). Since an analytical expression of $G_{HFCS}{}^{\Phi 0}$ (t*) seems out of range, $G_{HFCS}{}^{\Phi 0}$ (t*) was established from finite element (FE) simulations, achieved in COMSOL-Multiphysics software on a 2D axisymmetric model (see Figure 2). The COMSOL model solves the partial derivative equation (4), that is the normalized heat equation. An adiabatic condition was set on every domain face, except at the ground heat exchanger wall where a constant normalized power was set (Neumann condition). The size of the domain ($r \approx 2\sqrt{3\, t_{max}{}^*}$) was large enough to ensure it did not disturb the heat transfer in the borehole vicinity. The mesh was refined in the vicinity of the borehole wall to account for sharp temperature gradient, with typical length of the triangular elements being 2 cm. Note that a coarser mesh would have been appropriate, however, as the model is 2D, a fine mesh does not compromise the execution time.

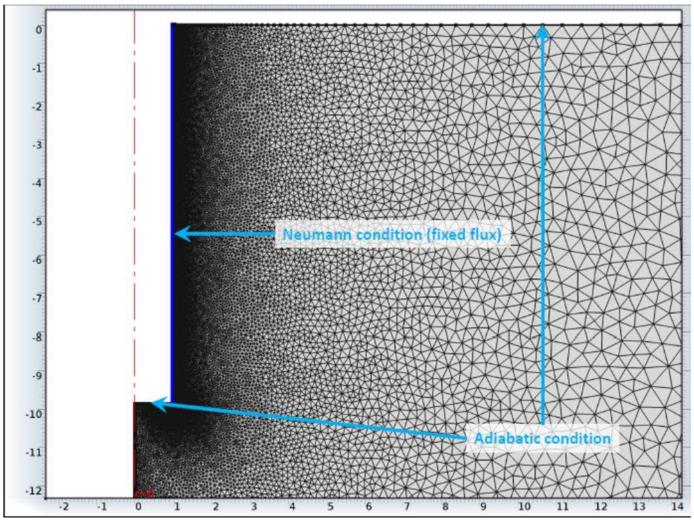

Figure 2: Mesh of the Finite Element model used to compute HFCS G-function. H*=10

The FE simulations were carried out for aspect ratio ranging from H* = 10 to 200. This covers radiuses up to 1 m for 10 m deep PHE, and radiuses ranging from 15 cm to 3,000 cm for a 30 m deep PHE. $G_{HFCS}^{\Phi 0}$ (t*) was computed through a parametric sweep encompassing 39 simulations (H* = 10, 15, ... , 195, 200). The response was obtained by averaging the temperature over the whole pile depth, evaluated at 109 normalized times t* ranging from 0 to 1.2×10^6, following a geometric progression to capture sharper changes at small time scales.

Figure 3 plots the results of the new $G_{HFCS}^{\Phi 0}(t^*)$ in comparison with the $G_{FLS}^{\Phi 0}(t^*)$. The G-function for the HICS is also included. Excellent agreement is reached between the analytical solution of the HICS and HFCS models at small times, and between FLS and HFCS for larger values of t*. This is due to the fact that HICS model correctly describes the temperature change close to pile early in the solicitation, while the FLS model accounts for axial heat transfer which play a more significant role later [43]. The difference between the FLS and the HFCS almost vanish after t* = 100 (Δ_{FLS}<2.5%).

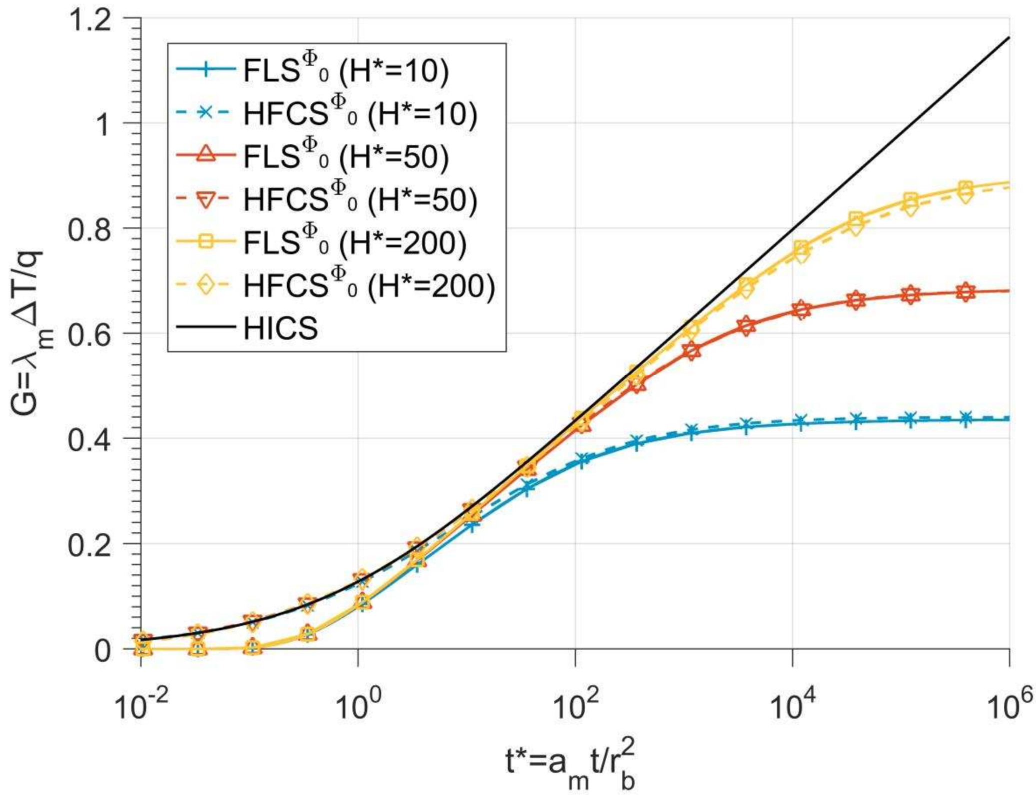

Figure 3: Comparison of finite line source FLS$^{\Phi 0}$ and hollow infinite cylindrical source models HICS to the newly developed hollow finite cylindrical source (HFCS$^{\Phi 0}$) step response, for three values of aspect ratio H*. All models include an adiabatic ground surface condition.

Hence, the newly developed HFCS$^{\Phi 0}$ G-function assuming adiabatic condition at the top surface is suitable for both short and long duration, accounting for both heat transfers close to the pile and vertical heat transfers. For practical applications an easy-to-use regression was established. It was based on 4251 evaluations of $G_{HFCS}(t^*)$ (39 values of H* × 109 values of t*), for $10^{-4} < t^* < 10^{6}$ and $10 < H^* < 200$:

$$G_{HFCS^{\Phi 0}}(H^*, t^*) = \frac{G_{max}}{2}\left(1 + \tanh\left(\sum_{n=1}^{3} A_n(H^*)\left(\log_{10}(t^*) - X(H^*)\right)^n\right)\right) \quad (6)$$

The five coefficients of the HFCS$^{\Phi 0}$ model G_{max}, X, A_1, A_2, A_3 are expressed as simple functions of the aspect ratio H*:

$$coefficient(H^*) = \sum_{k=1}^{4} a_k (\log_{10}(H^*))^{k-1} \quad (7)$$

The 20 coefficients of eq. (7) (4 coefficients a_i for every 5 parameter G_{max}, X, A_1, A_2, A_3) were determined by minimizing the misfit (root mean square error) between the 4251 evaluations of $G_{HFCS}(t^*)$ and eq. (6) with the fmincon function of Matlab®. For the five HFCS$^{\Phi 0}$ parameters, the coefficients a_1, a_2, a_3 and a_4 are given in Table 1.

	G_{max}	X	A_1	A_2	A_3
a_1	0.14902	0.23592	0.068755	-0.013467	-0.33526
a_2	1.2658	-0.14631	0.027615	0.69358	-0.048028
a_3	-0.070655	0.015128	0.0055503	0.016762	-0.009149
a_4	0.00082108	-0.010045	0.013457	-0.00057945	-0.00082768

Table 1: Regressions over the five coefficients of the HFCS model G_{max}, X, A_1, A_2, A_3, established for $10^{-4} < t^* < 1.2\times10^{6}$ and $10 < H^* < 200$.

The regression is able to reproduce the original dataset in an excellent way (Figure 4).

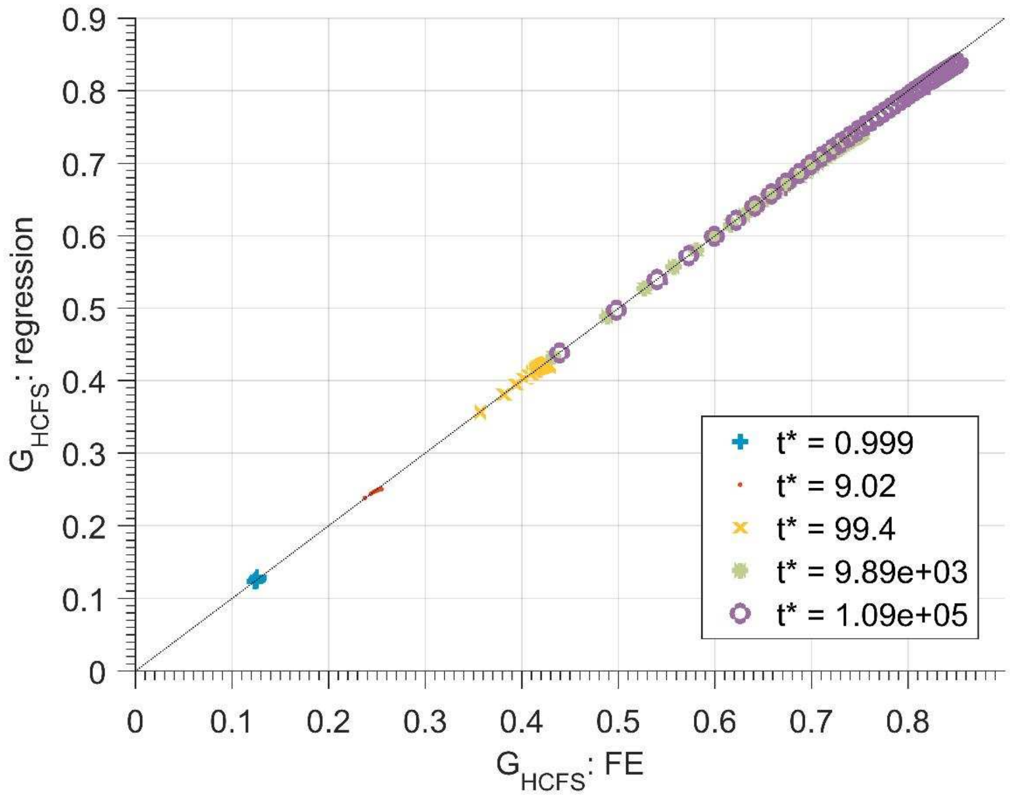

Figure 4: HCFS$^{\Phi 0}$-model: Comparison between the FE derived G-functions and the regression function (Equation 6) with fitted parameters (Table 1): G-function at different normalized times t* for *a* range of aspect ratios (H* = 10 to 200)

2.2. Resistive-capacitive circuit

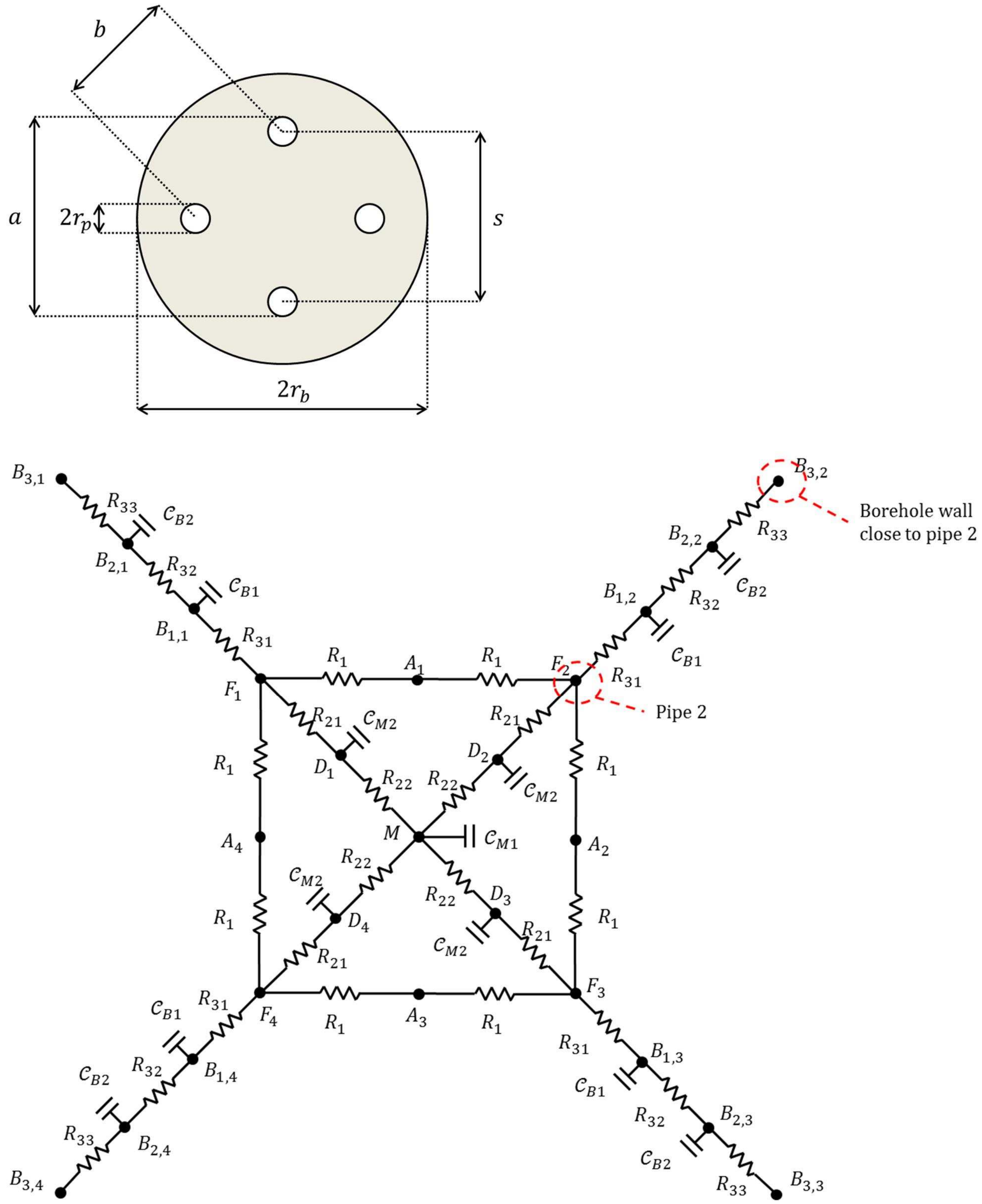

Figure 5: Modelled PHE cross-section (top) and developped RC circuit (bottom).

The RC model was developed for configurations with 4 pipes (Figure 5). Configurations with 2 pipes were not investigated as they seem to be unused in French PHE projects. It comprises six resistances (R_1, $R_{2,1}$, $R_{2,2}$, $R_{3,1}$, $R_{3,2}$, $R_{3,3}$) and four capacities (C_{B1}, C_{B2}, C_{M1}, C_{M2}). The number of resistances and capacities is a trade-off between accuracy and model complexity. The outer face of each pipe, denoted F_i (i=1,…,4) is connected to the adjacent portion of the heat exchanger wall $B_{3,i}$ by a serial connection of three resistances $R_{3,1}$, $R_{3,2}$, $R_{3,3}$. Two capacities C_{B1} and C_{B2} are inserted at the corresponding nodes. This outer portion of the circuit describes the temperature evolution in the outer part of the pile. Every pipe is connected to the central part of the pile by a two serial resistances $R_{2,1}$ and $R_{2,2}$ and a corresponding capacity C_{M2}. Finally, the central part of the pile is represented by its own capacity C_{M1}. Interactions between adjacent pipes (such as F_1 and F_2) are represented by two resistances R_1.

Normalized linear resistances R_i^* and linear capacities C_i^* are introduced:

$$R_i^* = \lambda_c R_i$$
$$C_i^* = \frac{1}{\left(\rho C_p\right)_c {r_b}^2} C_i \tag{8}$$

In eq. (8) λ and (ρC_p) respectively account for the ground thermal conductivity (W.K^{-1}.m^{-1}) and volumetric heat capacity (J.K^{-1}.m^{-3}) The resistances $R_1^* = R_{2,1}^* + R_{2,2}^*$ and $R_3^* = R_{3,1}^* + R_{3,2}^* + R_{3,3}$ are introduced along with three parameters x_2, y_2, y_3 to describe the location of $C_{B,1}^*$, $C_{B,2}^*$ and $C_{M,2}^*$:

$$x_2 = \frac{{R_{21}}^*}{{R_2}^*}$$
$$x_3 = \frac{{R_{31}}^*}{{R_3}^*} \tag{9}$$
$$y_3 = \frac{{R_{32}}^*}{{R_3}^*}$$

Coefficients R_j^* and C_i^* are functions of $r_p^*=r_p/r_b$, the normalized outer pipe radius, and $s^*= s/r_b$, the normalized centre-to-centre shank spacing respectively (Figure 5). They were identified by a numerical procedure described in Annex A for 181 configurations (Figure 6). To ensure geometrical constraints, such as no overlapping between pipes, the RC parameters were estimated for (r_p^*, s^*) fulfilling the three following constraints:

$$(c_1): {r_p}^* > 0.033$$
$$(c_2): s^* - 2\sqrt{2}{r_p}^* > 0.60 \tag{10}$$
$$(c_3): s^* + 2\,{r_p}^* < 1.73$$

The first constraint (c_1) ensures a minimum normalized pipe radius r_p^* while the second and third constraints (c_2 and c_3) respectively impose minimum and maximum normalized shank spacing s^*. Let us assume a typical pipe outer radius r_p = 1.6 cm. For r_b = 30.0 cm, r_p^* = 1.6/30.0 = 0.0533 and (c_1) is checked. Since s^* must be between 0.7508 (c_2) and 1.6233 (c_3), the RC parameters can be estimated from s = 0.7508 × 30.0 = 22.5 cm to 1.6233 × 30.0 = 48.7 cm. If r_b = 10 cm, then r_p^* = 1.6/10.0 = 0.160 and s must be between 10.5 cm and 14.1 cm.

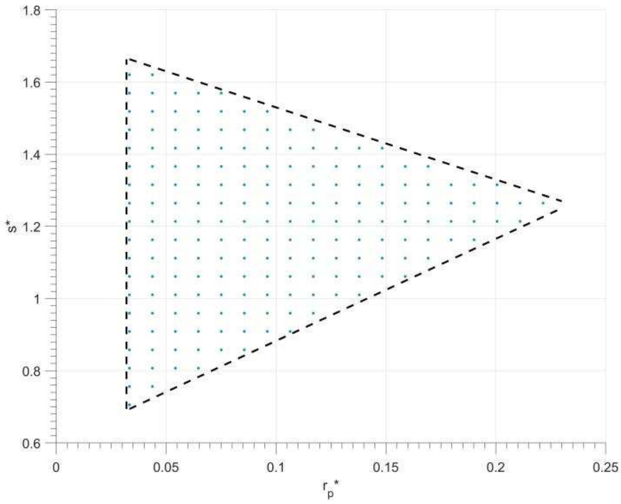

Figure 6: Domain of validity for RC parameters: r_p* and s* shall be within the triangle. Dots indicate the 181 configurations where the RC parameters where computed.

The supporting information of the article contains a table with the resistances R_1^*, R_2^*, R_3^* capacities C_{B1}^*, C_{B2}^*, C_{M1}^*, C_{M2}^* and locations x_2, x_3, y_3 at the 181 configurations. Graphical representation of every parameter is also included.

2.3. Implementation of the semi-analytical PHE model

A model coupling the HFCS $^{\Phi 0}$ G-function with the RC circuit was developed to compute the temperature evolution of the PHE heat-carrier fluid (cf. Figure 7). The model is qualified as "semi-analytical" (SA) since it couples the G-functions (the analytical part) with a numerical scheme to compute the temperature in the RC circuit (the numerical part).

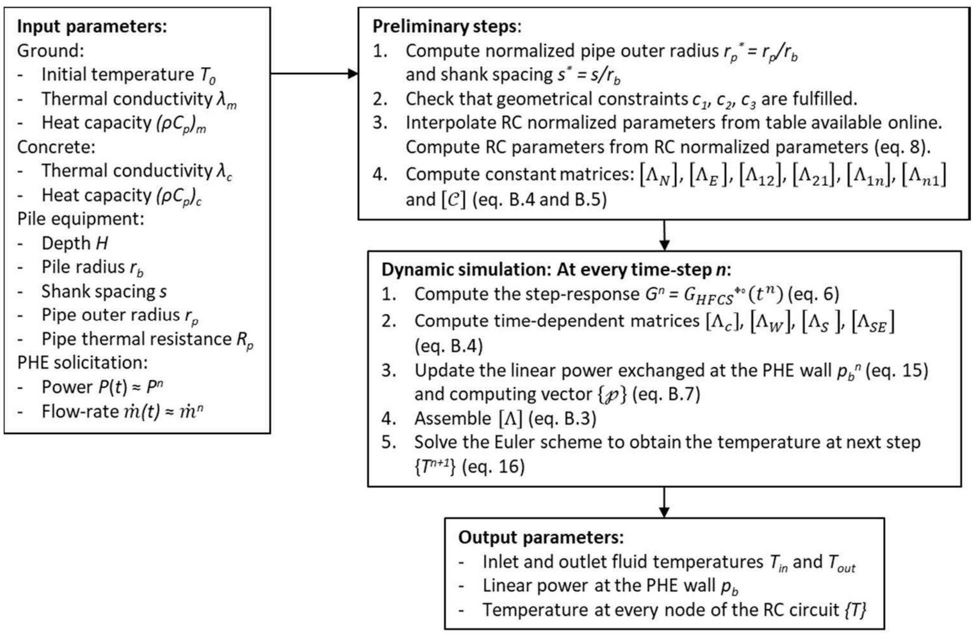

Figure 7: Flowchart with input/output parameters of the developed semi-analytical model. Equations (B.i) refers to annex B.

Time is discretized in n steps $t_n = n\,\Delta t$. The heat-carrier fluid feeds pipes 1, 2, 3 and 4. The 4 pipes are connected in series, since this matches observed engineering practices. Note that if other arrangements, e.g. parallel, are required, the RC parameters computed in the previous section remain appropriate. However, the matrices assembling procedures described in Annex B is no longer valid and should be modified.

A time-varying power P^n is applied to the heat-carrier fluid:

$$P^n = \dot{m}^n C_{p,fl}({T_{in}}^n - {T_{out}}^n) \tag{11}$$

With $\dot{m}^n$ the mass flow rate in the PHE (kg.s^{-1}), $C_{p,fl}$ the mass-specific heat capacity of the heat carrier fluid (J.K^{-1}.kg^{-1}), $T_{in}{}^n$ and $T_{out}{}^n$ respectively PHE inlet and outlet temperatures (°C).

The temperature at the PHE nodes is described by a vector $\{T^n\}$. This vector encompasses all the temperature in the RC circuit along with PHE inlet outlet temperatures. The temperatures are assumed to be constant upon the whole PHE depth (one temperature per pipe), though this assumption may be inaccurate for borehole heat exchangers [24,41,44]. For instance Zeng et al. models can predict fluid temperature along the depth [24]. For a short pile (H = 10 m) this assumption is validated by comparison with a 3D FE model which solves the fluid temperatures along the depth in every pipe (see 2.4). This assumption should be discussed for deeper PHE.

Heat exchange between the fluid in pipe i and the outer face of a pipe i is accounted for by an effective thermal resistance R_p (K.m.W^{-1}) accounting for the convection within the fluid R_{conv} and the pipe thermal resistance R_{p0}:

$$R_p = R_{conv} + \underbrace{\frac{1}{2\pi\lambda_p}\ln\left(\frac{r_p}{r_{p,i}}\right)}_{=R_{p0}} \tag{12}$$

λ_p and $r_{p,i}$ are the pipe thermal conductivity and inner radius respectively. R_{conv} has been computed by correlations reported in [45]. Establishing a heat balance at the nodes of the RC circuit leads to a differential equation on $\{T^n\}$:

$$[\mathcal{C}]\frac{d}{dt}\{T\} + [\Lambda]\{T\} = \{\wp\} \tag{13}$$

$[\mathcal{C}]$, $[\Lambda]$ and $\{\wp\}$ are respectively a capacitance matrix (J.K^{-1}.m^{-1}), a conductance matrix (W.K^{-1}.m^{-1}) and a linear power vector (W.m^{-1}). Their expressions are given in Annex B.

Here is the key point to couple the analytical model with the numerical model. The pile wall temperature T_p is computed through the superposition principle [18]:

$$ {T_P}^n - T_0 = \frac{1}{\lambda_m}\left({p_b}^1 G^n + \sum_{l=1}^{n-1}\left({p_b}^{l+1} - {p_b}^{l}\right)G^{n-l}\right) \tag{14}$$

Where p_b is the linear power (or power by unit length of pile) exchanged at the PHE wall (W.m^{-1}), which is supposed to be constant along the depth, and T_p the temperature at this node. All the nodes $B_{3,i}$ are connected to the PHE wall, leading to:

$$p_b{}^n = \sum_{i=1}^{4} \frac{T_{B2,i}{}^n - T_p{}^n}{R_{33}} \tag{15}$$

$\{T^{n+1}\}$ is determined by solving equation (13) with an implicit Euler scheme implemented in Matlab®, which results in the following linear system:

$$[\mathcal{C}]\frac{\{T^{n+1}\} - \{T^n\}}{\Delta t} + [\Lambda]\{T^n\} = \{\wp\}$$
$$\Rightarrow \left(\frac{1}{\Delta t}[\mathcal{C}] + [\Lambda]\right)\{T^{n+1}\} = \frac{1}{\Delta t}[\mathcal{C}]\{T^n\} + \{\wp\} \tag{16}$$

The influence of time step on the temperature precision was investigated for Δt ranging from 0.25 h to 1 h. The tested configuration is similar to case a presented in section 2.4, except that the 500 W power is applied for 6 h followed by 6 h of relaxation (cf. Figure 8). The implicit Euler scheme has proven to be stable. Temperatures computed for Δt = 0.25 h and 0.5 h are almost superposed, suggesting that a 0.25 h time step is unnecessary small. Δt = 1 h can lead to an underestimation of the temperature change when the power changes sharply by c.a. 0.7 °C. Given this, Δt = 0.5 h is a good starting point to run the SA model, and the authors recommend to test the influence of Δt on the result precision.

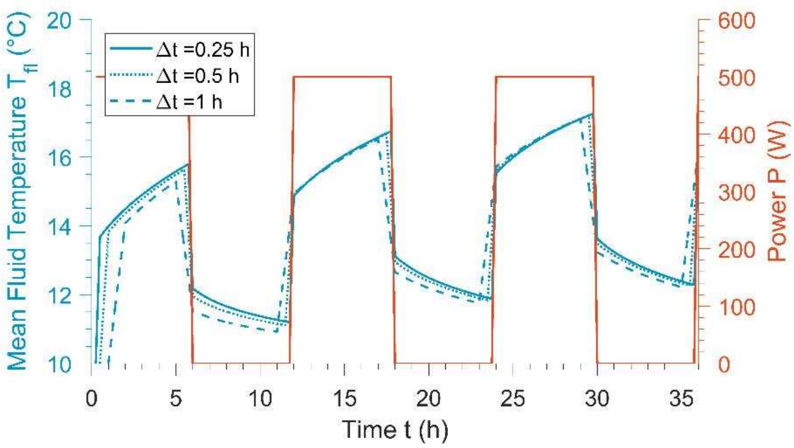

Figure 8: Influence of time step for *a* periodic solicitation.

The main advantage of the semi-analytical model is that its execution is fast. For instance, evaluation of 1 000 time-step requires about 10 s on a desktop PC. Its implementation requires no advanced skills in programming and could be implemented in open software like Python, given the detailed flowchart (Figure 7). In the author's view, the most significant shortcoming of the SA model is that it considers a single PHE with an adiabatic condition at the surface, corresponding to a building of infinite extension whose floor is perfectly insulated. Recent research shows how the ground thermal regime is affected by the boundary condition at the surface [46–48]. Further development of the SA models will cope with multiple PHE with more realistic boundary conditions. Another shortcoming is that the model holds only for 4 pipes.

2.4. Model validation against FE code

The SA model was validated against a finite element (FE) model developed in COMSOL-Multiphysics® software for 5 cases (Table 2). For all simulations the PHE was 10 m deep and a linear constant power 50 $W.m^{-1}$ was applied. The parameters used in the simulation are summarized in Table 3. The initial temperature was set to T_0 = 0°C. The flow is turbulent; as a result, the convective thermal resistance is an order of magnitude lower than the conductive one.

Validation case	Pile radius r_b (cm)	Distance between two opposite pipes s (cm)	Concrete thermal conductivity ($W.K^{-1}.m^{-1}$)	Dimension of the FE model	Simulation time
a	30	30	1.2	2D	200 h
b	30	40	1.2	2D	200 h
c	30	30	1.8	2D	200 h
d	30	40	1.8	2D	200 h
e	30	30	1.8	3D	5.0 y

Table *2 :* Cases used for the validation of the semi-analytical model

Pipe characteristics					Solicitation		
External pipe radius	Internal pipe radius	Pipe thermal conductivity	Pipe resistance	Effective pipe resistance	Mass flow-rate		Power
r_p = 10 mm	$r_{p,i}$ = 2.5 mm	λ_p = 0.40 W.K-1.m-1	R_{p0} = 0.0776 K.m.W-1	$R_p = R_{p0} + R_{conv}$ = 0.089 K.m.W-1	$\dot{m}$ = 0.1 kg.s-1		P = 500 W
Fluid characteristics and flow conditions							
Heat capacity	Dynamic viscosity[a]	Thermal conductivity[a]	Prandtl number[a]	Nusselt number	Reynolds number	Flow regime	Convective resistance
$C_{p,fl}$ = 4180 kJ.kg-1.m-3	ν_{fl} = 1.31 mPa.s	λ_{fl} = 0.578 W.K-1.m-1	Pr = 9.47	Nu = 48.21	Re = 5925	Turbulent	R_{conv} = 0.0114 K.m.W-1
Ground characteristics						**Concrete characteristics**	
Thermal conductivity			Volume-specific heat capacity			Volume-specific heat capacity	
λ_m = 2.3 W.K-1.m-1			$(\rho C_p)_m$ = 2.4 MJ.K-1.m-3			$(\rho C_p)_c$ = 2.16 MJ.K-1.m-3	
[a]: Computed with CoolProps tool at a reference temperature of 10 °C (http://www.coolprop.org/)							

Table 3 : Parameters common to all validations of the semi-analytical model

The fluid in every pipe is modelled in one dimension along the pipe axis s. A power balance (W) on an elementary volume V of fluid contained between s and s+ds reads:

$$\int \frac{De}{Dt} d\mathcal{V} = \oint \underline{\phi}.\underline{dS} \tag{17}$$

In eq. (17), D/Dt is the material (lagragian) derivative. The term in the left accounts for the variations of fluid energy per volume e (J.m-3):

$$\int \frac{De}{Dt} d\mathcal{V} = \int \frac{D(\rho_{fl} C_{p,fl} T_{fl})}{Dt} d\mathcal{V} = \rho_{fl} C_{p,fl} \left(\frac{\partial T_{fl}}{\partial t} + v \frac{\partial T_{fl}}{\partial s} \right) \pi r_{p,i}{}^2 ds$$
$$= \pi r_{p,i}{}^2 \, ds \, \rho_{fl} C_{p,fl} \frac{\partial T_{fl}}{\partial t} + \dot{m} C_{p,fl} \frac{\partial T_{fl}}{\partial s} ds \tag{18}$$

In eq. (18), ρ_{fl} is the fluid density (kg.m-3), and v the fluid velocity (m.s-1), given that:

$$\dot{m} = \rho_{fl} \, v \, (\pi r_{p,i}{}^2) \tag{19}$$

The term in the right of eq. (17) accounts for the incoming flux from the outer side of the pipe at temperature T_p to the fluid through conduction in the pipe and advection:

$$\oint \underline{\phi}.\underline{dS} = \frac{T_p - T_{fl}}{R_p} ds \tag{20}$$

Combining eq. (18) and (20), the heat balance (17) can be rewritten:

$$\pi r_{p,i}{}^2 \, \rho_{fl} C_{p,fl} \frac{\partial T_{fl}}{\partial t} + C_{p,fl} \dot{m} \frac{\partial T_{fl}}{\partial s} + \frac{T_{fl} - T_p}{R_p} = 0 \tag{21}$$

As the heat-carrier fluid volume is negligible compared to the concrete volume, the thermal inertia of the fluid is overlooked, which results in:

$$\dot{m}C_{p,fl}\frac{\partial T_{fl}}{\partial s}+\frac{T_{fl}-T_p}{R_p}=0 \tag{22}$$

Cases a, b, c and d focus on transient thermal effects within the pile over t = 200 h. Since the deviation between HICS and HFCS model is low, vertical heat transfers are expected to play only a small role on the fluid temperature evolution. Therefore, the benchmark was run with a 2D horizontal FE model against the SA model with the HICS G-function. The 2D FE model considers independent fluid and pipe temperature $T_{fl,i}$ and $T_{p,i}$, as does the SA model. In the 2D FE model, eq. (22) is integrated over every pipe i from the pipe inlet to the pipe outlet:

$$\begin{gathered}\dot{m}C_{p,fl}\frac{\left(T_{fl,i}-T_{fl,j}\right)}{H}+\frac{1}{R_p}\left(\left(\frac{T_{fl,i}+T_{fl,j}}{2}\right)-T_{p,i}\right)=0\\ T_{fl,j}=\begin{cases}T_{fl,4}+\dfrac{P}{\dot{m}C_{p,fl}} & \text{if } i=1\\ T_{fl,i-1} & \text{if } i=2,3,4\end{cases}\end{gathered} \tag{23}$$

In eq. (23), R_p is the effective thermal resistance defined by eq. (12). In the given pipe i, the coupling term (second term) is evaluated at the mean fluid temperature.

Case e tests the ability of the SA model to account both for transient thermal heat transfer within the pile and vertical heat transfer in the ground, over a long duration t = 5 years (t* =1679). Since the pile aspect ratio is H* = 10/ 0.3 = 33.3, the HICS model overestimates the step response by 20% compared to HFCS model. Therefore, vertical heat transfers are expected to play a role on the fluid temperature evolution. Consequently a 3D FE model was used. The fluid temperature $T_{fl,i}(s,t)$ in pipe i is along the the pipe abscise s. The resolution of eq. (22) is implemented with linear extrusion operators in COMSOL-Multiphysics 4.2a, which allow the averaging of pipe temperature around polar coordinate θ at a given location s:

$$\dot{m}C_{p,fl}\frac{\partial T_{fl,i}}{\partial s}+\frac{1}{2\pi R_p}\int_{\theta=0}^{2\pi}\left(T_{fl,i}-T_{p,i}\right)\mathrm{d}\theta=0 \tag{24}$$

For both 2D and 3D models, the mesh is refined is the vicinity of the pipes (see Figure 9), and COMSOL solves the heat equation (2) in the solid parts, i.e. concrete and ground.

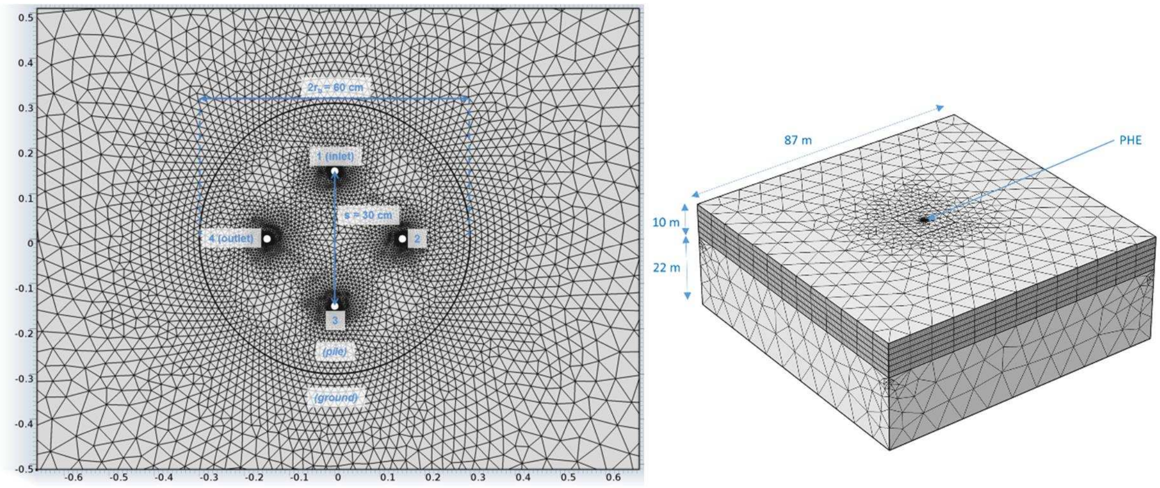

Figure 9: Mesh of FE model used for SA model validation: 2D model (case *a* to d, left) and 3D model (case e, right)

The SA model was run with a time step Δt = 1h and its heat balance was checked. The sum of the internal power of the concrete and the power transferred at the borehole wall equals the linear power given by the fluid (50 $W.m^{-1}$).

The SA and FE models are in good to excellent agreement for medium-term simulations (cases a to d) (see Figure 10). The SA model slightly underestimates the change in mean fluid temperature between approximately one hour and 25 hours. In the worst case (a), the SA model underestimates the temperature by 0.4 °C. The discrepancy is largest with lower concrete thermal conductivity, possibly suggesting that the R-C circuit is not 100% capturing the concrete capacity in the very short term. There may also be a small difference related to the use of the cylindrical source in the SA model which assumes application of the heat at the edge of the pile rather than within it. At longer times heat transfer to the ground becomes predominant and the SA and FE elements models give the same temperature evolution. Case c has the lowest long-term temperature evolution since the pipes are remote (s = 40 cm). This reduces the thermal short-circuit between the pipes. Overall, given the small discrepancies between the SA and FE solutions, this comparison validates the RC circuit along with the implementation of the semi-analytical model.

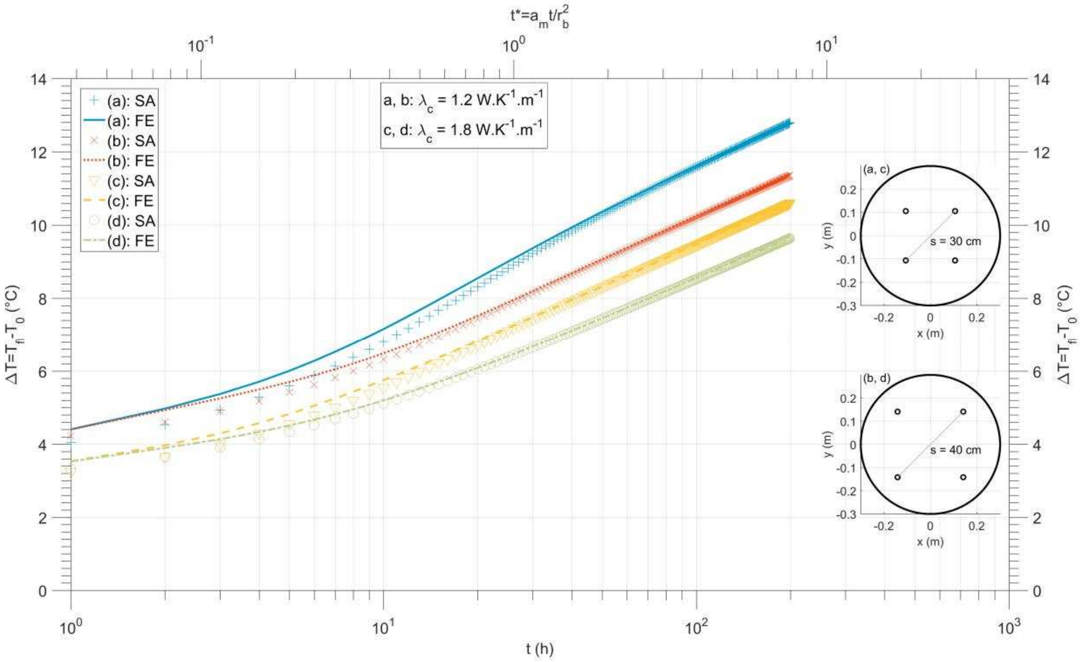

Figure 10: Benchmark of SA model against FE model: Change in the mean fluid temperatures. Cases a, b c and d

For the long-term simulation (case e), the agreement between the SA and the FE model is also excellent, both for inlet/oulet temperatures and temperature distribution in the pipes (see Figure 11 and Figure 12). From a numerical point of view, this validates the SA model for the short to long-term computation of the fluid temperature, from one hour to several years.

However the adiabatic condition imposed on the surface means that the ground and the building above the pile are assumed to exchange no heat. Further research work is needed to confirm the appropriateness of this assumption. Note that as the power exchanged was kept constant (500 kW), the time step chosen by the FE model solver grown exponentially, resulting in a reasonable execution time (about 3 h for 5 years). In case of more realistic time-varying solicitation, the time step would collapse, resulting in an execution time not compatible with engineering practices.

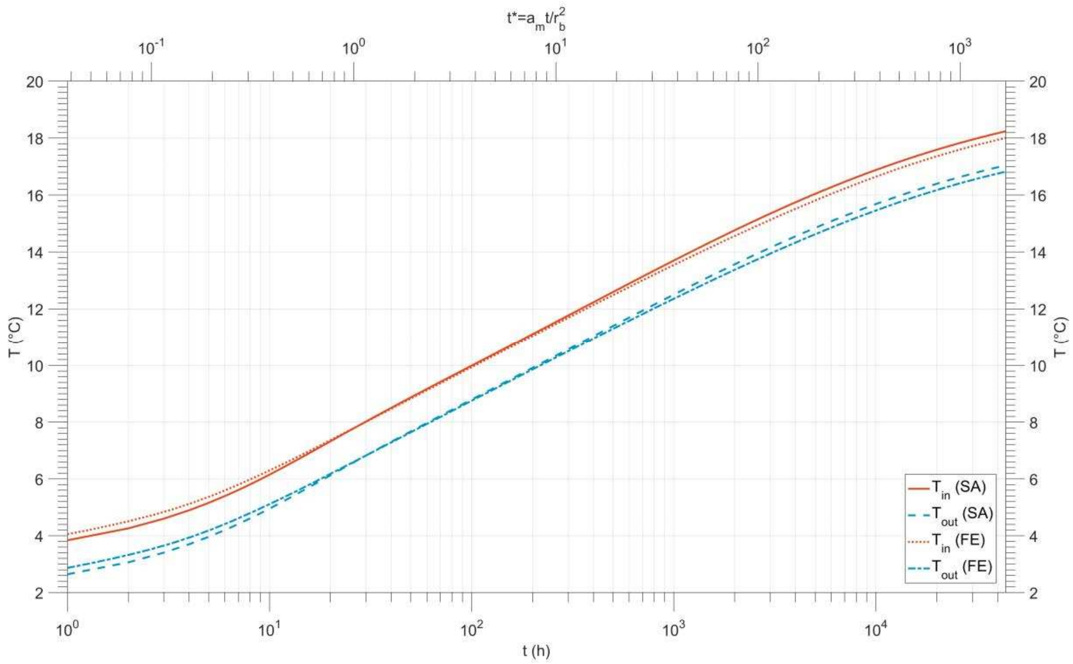

Figure 11: Benchmark of SA model against FE model: Change in PHE inlet and outlet temperatures. Case *e*

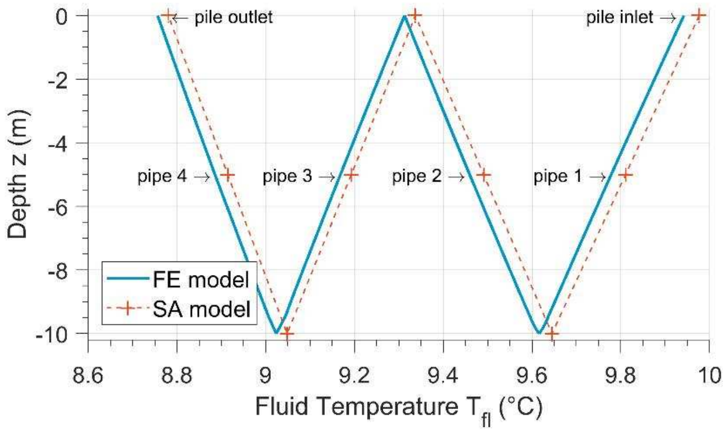

Figure 12: Comparison of vertical profiles of fluid temperature at t = 100 h. Crosses at mid-depth refer to the mean fluid temperature variables $T_{fl,1}$ to $T_{fl,4}$ (see annex 2) in the SA model. Crosses at one pipe end refer to $T_{fds,i}$

3. Comparison of the SA model to models without concrete capacity

Models which neglect the thermal inertia of the pile concrete (purely resistive models, or 1R) are often used to predict the evolution of fluid temperature. They account for the thermal transfer in the ground heat exchanger by a single resistance R_b, while the heat transfer in the ground is modelled by the FLS, ILS or HICS models.

The influence of this assumption was investigated by comparing the new SA model with R-C circuit to a state of the art model used commonly for BHE, namely the FLS with steady state resistance, R_b. For consistency both the FLS and the FHCS used in the SA model were applied using an adiabatic condition at the ground surface.

The range of conditions investigated included pile radius r_p of 15 and 30 cm, shank spacing s ranging from r_b to 1.33 r_b, low and high values of ground and concrete thermal conductivities, respectively λ_m = 1.3 W.K^{-1}.m^{-1} and 2.3 W.K^{-1}.m^{-1}, λ_c = 1.2 W.K^{-1}.m^{-1} and 1.8 W.K^{-1}.m^{-1} (Table 4). The initial temperature was set to T_0 = 10 ℃. The other parameters remained the same as for the validation case (Section 2.3). The temperature evolution was simulated for 200 h to focus on the effect of transient heat transfer in the pile on the temperature evolution.

Input data						Output data
Case	r_b (cm)	s (cm)	λ_m ($W.K^{-1}.m^{-1}$)	λ_c ($W.K^{-1}.m^{-1}$)	R_b ($K.m.W^{-1}$)	$T_{fl,1R\text{-}FLS}$ - $T_{fl,SA}$ at t = 1 h (°C)
1	15	15	2.3	1.8	0.096	1.385
2	15	17.5	2.3	1.8	0.086	0.983
3	15	20	2.3	1.8	0.077	0.593
4	30	30	2.3	1.8	0.112	2.378
5	30	35	2.3	1.8	0.102	1.801
6	30	40	2.3	1.8	0.093	1.305
7	15	15	1.3	1.8	0.096	1.261
8	15	17.5	1.3	1.8	0.086	0.853
9	15	20	1.3	1.8	0.077	0.454
10	30	30	1.3	1.8	0.112	2.376
11	30	35	1.3	1.8	0.102	1.799
12	30	40	1.3	1.8	0.093	1.302
13	15	15	2.3	1.2	0.134	2.524
14	15	17.5	2.3	1.2	0.118	1.856
15	15	20	2.3	1.2	0.104	1.237
16	30	30	2.3	1.2	0.158	3.820
17	30	35	2.3	1.2	0.142	2.916
18	30	40	2.3	1.2	0.128	2.160
19	15	15	1.3	1.2	0.134	2.409
20	15	17.5	1.3	1.2	0.118	1.736
21	15	20	1.3	1.2	0.104	1.110
22	30	30	1.3	1.2	0.158	3.819
23	30	35	1.3	1.2	0.142	2.915
24	30	40	1.3	1.2	0.128	2.158

Table *4 :* Cases used for the comparison between the 1R and SA models

As indicated, the purely resistive (1R) model was built by connecting the mean fluid temperature $T_{fl,1R}$ to the ground heat exchanger wall at temperature T_p via a steady-state thermal resistance R_b. The linear power transferred to the ground p reads:

$$p = \frac{T_{fl,1R} - T_p}{R_b} \tag{25}$$

R_b was estimated assuming a homogenous fluid temperature in the PHE. Consequently no heat is transferred between pipes and resistances R_1. $R_{2,1}$ and $R_{2,2}$ don't play any role. 4 resistances ($R_{3,1}$+$R_{3,2}$+$R_{3,3}$+R_p) connect the fluid ($T_{fl,1R}$) to the borehole wall (T_p). R_b reads:

$$R_b = \frac{R_{3,1} + R_{3,2} + R_{3,3} + R_p}{4} \tag{26}$$

Combining (25) with the FLS G-function leads to:

$$T_{fl,1R} = T_0 + pR_b + \frac{p}{\lambda_m} G(t) \tag{27}$$

3.1. Comparison Results

After 1 hour of operation, the temperature discrepancy between 1R-FLS and SA models $\Delta T = T_{fl,1R,FLS} - T_{fl,SA}$ ranges between 0.46 °C (case 9) and 3.82 °C (case 16) as shown in Table 4. Approximating the PHE by a single resistance always leads to overestimations of the temperature changes of the heat-carrier fluid. In other words the performances of the PHE are always underestimated; no matter the pile radius, pipe spacing, concrete and ground thermal conductivities

The main results of the comparison are summarised below:

- Both SA and 1R-FLS models converge to the same function. It is expected since both models assume the same boundary condition, a perfect insulation, at the surface (see Figure 13 *a* and b).

- The temperature evolution for configurations with remoter pipes (s = 1.25 rb) is always below the temperature for configurations with closer pipes (s = 4/3 rb) (see Figure 13 *a* and b). The discrepancy between the IR-FLS and the SA models are larger when the pipes are closer. The extreme case is for r_b = 30 cm and s = 30 cm: the 1R-FLS model then overestimates the temperature change after 1h per 3.82 °C (see Figure 13 *a* and b).

- The long-term trend is reached at shorter times for smaller PHE than for larger PHE (see Figure 13 a and b). For the small radius (i.e. r_b = 15 cm), it takes c.a. 10 h (s = 20 cm) to 20 h (s = 15 cm) for both models to converge, while it requires approximately c.a. 50 h (s = 40 cm) to 100 h (s = 30 cm) for the large radius (r_b = 30 cm). The importance of the heat transfer within the concrete at the beginning of the analysis illustrates this observation. 2 hours are necessary for the concrete of smaller PHE to be half-loaded, i.e. to reach p_c = 25 W.m^{-1}, while it takes 10 hours for larger PHE to do so (see Figure 13 c).

- For the large PHE, the ground thermal conductivity λ_m has no effect on the temperature evolution up to 10 h (see Figure 13 d). Note that for narrower piles, the ground conductivity will play a role much earlier.Once the pile concrete is loaded, the slope of the curve is determined by λ_m, lower values of λ_m yielding to larger temperature changes.

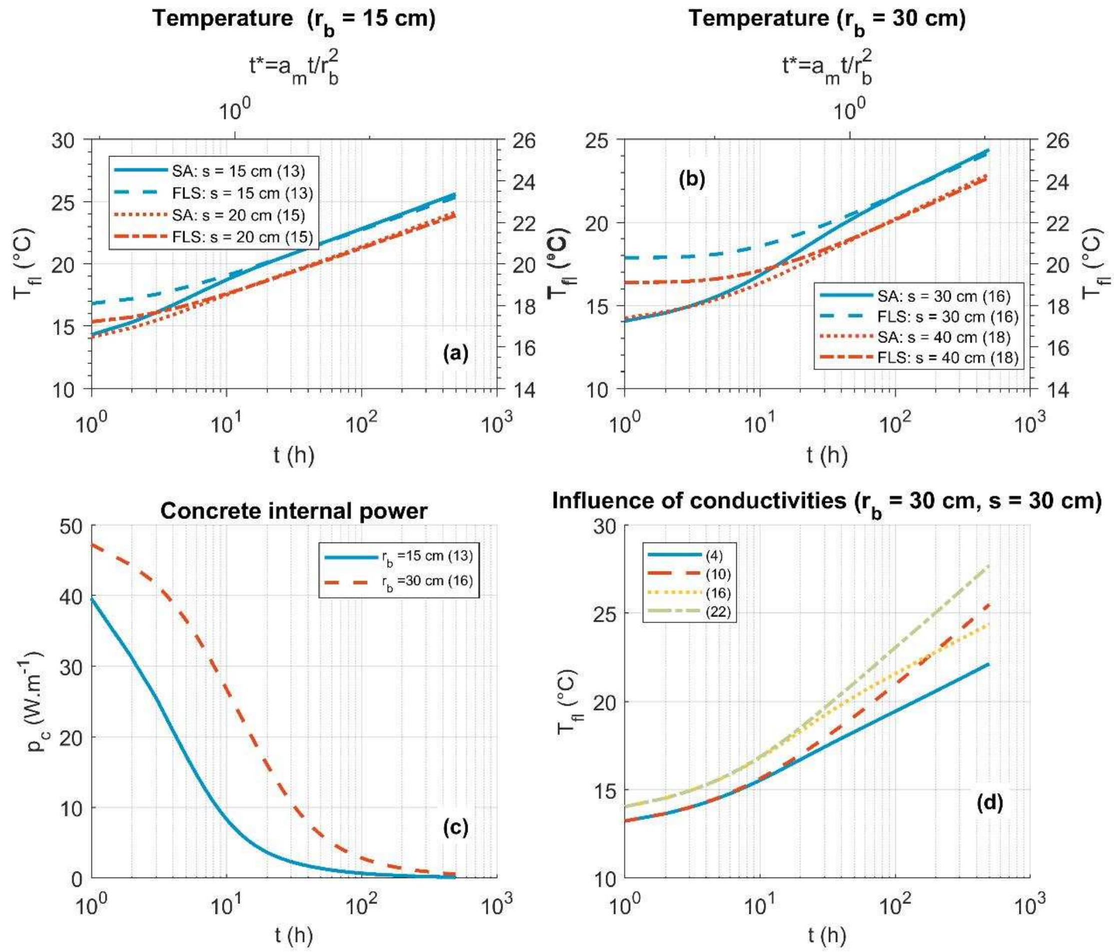

Figure 13: Main results of the comparison of the SA model to *a* model without concrete capacity. Temperature evolution refers to the evolution of the averaged inlet/outlet temperature.

These observations highlight that oversimplifying thermal transfers within the PHE always lead to overestimation of the temperature changes of the heat-carrier fluid and hence also underestimation of the capability of the pipes to transfer heat to the PHE and the ground. Models accounting for the pile thermal inertia offer the possibility to optimize the PHE performances and operations.

4. Application to TRT data

The SA model was applied to the analysis of a long thermal response test (TRT) carried out on a PHE with a radius of 30 cm and four heat exchange pipes installed, located in London clay, (cf. Table 5, Table 6 and Figure 14). The TRT lasted for 353 hours (14.7 days, see Table 6). Given the short duration of the test ($t^* < 10$), the boundary condition (adiabatic or isotherm) plays a negligible role over the TRT duration on the G-function. An adiabatic condition at the surface was assumed, and $G_{HFCS^{\Phi 0}}$ used (eq. (6)) in the SA model.

No laboratory measurement of ground and concrete thermal properties was performed, and the determination of distance between pipes s was based on standard construction details rather than as built records. The initial ground temperature T_0 was estimated by measuring the temperature of the heat-carrier fluid (water) circulating in the PHE before the TRT heater is switched on.

Ground properties		**PHE properties**					
Lithology	Initial temperature T_0 (°C)	PHE depth H (m)	Pile radius r_b (cm)	Distance between pipes s (cm)	Pipe outer radius r_p (mm)	Pipe thickness e_p (mm)	Thermal conductivity of the pipe λ_p ($W.K^{-1}.m^{-1}$)
London Clay	14.2	31	30.0	42.5	12.5	2.2	0.4

Table *5* : TRT: Characteristics of the ground and PHE

Fluid	Power P (kW)	Flow-rate $\dot{m}$ ($kg.s^{-1}$)	Temperature difference inlet/outlet ΔT (°C)
Water	1.69	0.32	1.25

Table *6* : TRT: Characteristics of the solicitation

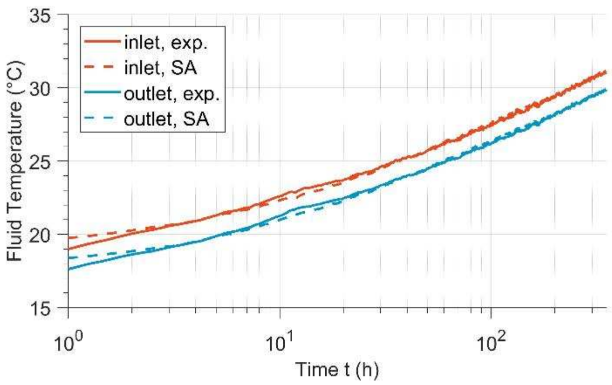

Figure 14: Evolution of PHE inlet and outlet temperatures monitored during the TRT, and SA model results (parameters fitted with $t_{min} = 1$ h, $t_{max} = 350$ h).

The ground volume-specific heat capacity was estimated based on SIA-384/6 guidelines [49] which indicates $(\rho C_p)_m$ in the range 2.0-2.8 $MJ.K^{-1}.m^{-3}$ for wet clay. A value $(\rho C_p)_m = 2.4$ $MJ.K^{-1}.m^{-3}$ was used. For the concrete $(\rho C_p)_c = 2.2$ $MJ.K^{-1}.m^{-3}$ was assumed.

The ability of the semi-analytical model to predict the fluid temperature evolution once the model parameters have been fitted was tested. Along with the ground thermal conductivity λ_m, the concrete thermal conductivity λ_c was chosen as an effective parameter accounting for internal thermal transfers within the pile.

Therefore, the TRT was interpreted by minimizing the root mean square error (RMSE) (°C) between measured and computed outlet temperatures was minimized [50] [51]:

$$RMSE(\lambda_m, \lambda_c) = \sqrt{\frac{\int_{t_{min}}^{t_{max}} \left(T_{out,exp}(t) - T_{out,SA}(\lambda_m, \lambda_c, t)\right)^2 dt}{t_{max} - t_{min}}} \quad (28)$$

The RMSE was minimized with the local optimization algorithm active-set developed in MATLAB®. The SA model was run with a time step Δt = 15 min, which ensured its evaluation within a few seconds.

The choice of the TRT duration should result from a compromise between the limitations of costs, leading to shorter TRT, and the reliability of the results, leading to longer TRT. Therefore, the influence of the value of the lower and upper bounds, respectively t_{min} and t_{max} upon λ_m and λ_c was investigated. The following values were used: t_{min} = 1, 5, 10, 20, 40 h and t_{max} = 100, 150, 200, 250, 300 and 350, making overall 30 simulations.

Note that the intrinsic ground and concrete thermal conductivities are constant values independent upon the investigation duration. However, the value of effective thermal conductivities derived from the TRT analysis will depends on how much of the test data is included in the analysis. Therefore these effective thermal conductivities appears to vary with the amount of time elapsed in the test. When this variation stops and the value of thermal conductivity converges on an asymptote, then one can be confident you that appropriate values have been fitted.

The estimated ground and concrete conductivities λ_m and λ_c tend to converge to values of 1.48 W.K^{-1}.m^{-1} and 0.94 W.K^{-1}.m^{-1} when t_{max} increases. Meanwhile, the dependence upon t_{min} tends to decrease (Figure 15). For instance, for t_{max} = 100 h, λ_m ranges between 1.63 W.K^{-1}.m^{-1} (t_{min} = 40 h) and 1.86 W.K^{-1}.m^{-1} (t_{min} = 1 h), leading to a difference of 0.23 W.K^{-1}.m^{-1}. However, when t_{max} = 350 h, λ_m ranges between 1.44 W.K^{-1}.m^{-1} (t_{min} = 40 h) and 1.51 W.K^{-1}.m^{-1} (t_{min} = 1 h), with a difference of only 0.07 W.K^{-1}.m^{-1}. As time increases, the estimated thermal ground thermal conductivity tends to be independent upon the lower bound of integration t_{min}. Furthermore, negligible change in λ_m and λ_c (≈ 1%) is observed between t_{max} = 250 h and t_{max} = 350 h.

The prediction of the SA model was compared to the prediction of a "classical" model for the interpretation of TRT on BHE (an approximation of the ILS G-function), which reads [52]:

$$T_{fl,cl} = T_0 + p\left[R_b + \frac{1}{4\pi\lambda_m}\left(\ln\left(\frac{4\lambda_m}{(\rho C_p)_m {r_b}^2}\right) - \gamma\right)\right] + \frac{p}{4\pi\lambda_m}\ln(t) \quad (29)$$

This model is valid for normalized time (Fourier number) $t^* > t_{min}^*$. The common criteria $t_{min}^* = 5$ was used [52]. The ground thermal conductivity λ_m determined from the classical interpretation is in the range 1.35 to 1.45 W.K^{-1}.m^{-1} while the thermal resistance R_b is between 0.128 and 0.134 K.m^{-1}.W^{-1} (see Table 7). Note that both λ_m and R_b increases when t_{max} increases from 250 to 350 h.

Reasons may be that the concrete is not fully loaded. The interpretation with the SA model yields λ_m = 1.45 to 1.50 W.K^{-1}.m^{-1}. For the longest integration time (t_{max} = 350 h), the SA gives a higher value of λ_m by approximately 3% to 6%. The larger range of values obtained for the classical ILS model suggest that a larger duration of data is required to use this approach. However, there is a trade off since use of the ILS based interpretation over longer timescales will lead to errors due to neglecting the importance of axial effects with short aspect ratio piles.

The SA model fits the concrete thermal conductivity rather than the pile thermal resistance. However, the latter can be calculated from the former, e.g. by the method of shape factors [53]. The values also rise with time as the thermal load on the concrete increases. As with λ_m, the values are slightly higher than that obtained from the classical ILS interpretation. The R_b values are slightly higher than might have been expected, but reflect the low thermal conductivity of the pile concrete and the relatively small number of heat exchange pipes installed.

"Classical" interpretation (eq. (29))						Interpretation with SA model				
t_{min}*	t_{min} (h)	t_{max} (h)	λ_m (W.K^{-1}.m^{-1})	R_b (K.m^{-1}.W^{-1})		t_{min} (h)	t_{max} (h)	λ_m (W.K^{-1}.m^{-1})	λ_c (W.K^{-1}.m^{-1})	R_b (K.m^{-1}.W^{-1})
5	200	250	1.35	0.128		40	250	1.45	0.96	0.137
5	200	300	1.38	0.129		40	300	1.43	0.97	0.138
5	200	350	1.42	0.132		40	350	1.43	0.97	0.138
7	260	350	1.45	0.134		1	350	1.50	0.93	0.141

Table *7 :* Comparison of the methods of TRT interpretation. In the interpretation with SA model, R_b is calculated based on λ_c and method of shape factors described in [53].

For PHE design it is also important to have accurate predictions of the outlet temperature since this effects the heat pump efficiency. To investigate this, the actual and simulated outlet temperatures are plotted in Figure 16 when t_{max}=250 hours with the SA model and the 1R-FLS model. For the latter model the ground value λ_m = 1.45 W.K^{-1}.m^{-1} and resistance R_b = 0.134 K.m^{-1}.W^{-1} are used. After the parameters have been fitted to the earlier test data, the predictions over the later test data (250 h < t < 350 h) are shown. The temperatures computed by the classical model and the SA model with t_{min} = 40 h are almost superposed. The SA model with parameters fitted on t_{min} = 1 h slightly underestimate the temperature by ≈ 0.2 °C. From a practical point of view, the classical model with parameters fitted t_{min}* = 5 predicts the overall temperature evolution well. However, the usefulness of the SA model lies in shorter times: while the 1R-FLS model overestimates the fluid temperature by 2.9 °C at t = 1h, the overestimation by the SA model is only 0.4 °C, and rapidly reduces. The SA model also reproduces the fluctuations in temperature that occur due to power input variations in a way a constant resistance model never can. This means the SA model is more suitable for use in routine operation when the supplied power varies over short timescales.

These results suggest that for this 30 cm wide PHE the SA model can be inverted to obtain reliable values of λ_m and λ_c, if the minimum TRT duration is 250 h (t* ~ 6.25). The SA model is then capable of reproducing the whole sequence of temperature, from short times (t ≈ 1 h) to longer times (250 h < t < 350 h), and could consequently be used for the dynamic simulations of PHE coupled to heat pumps. Larger errors would be expected at both short and long timescales based on the classical 1R-ILS model.

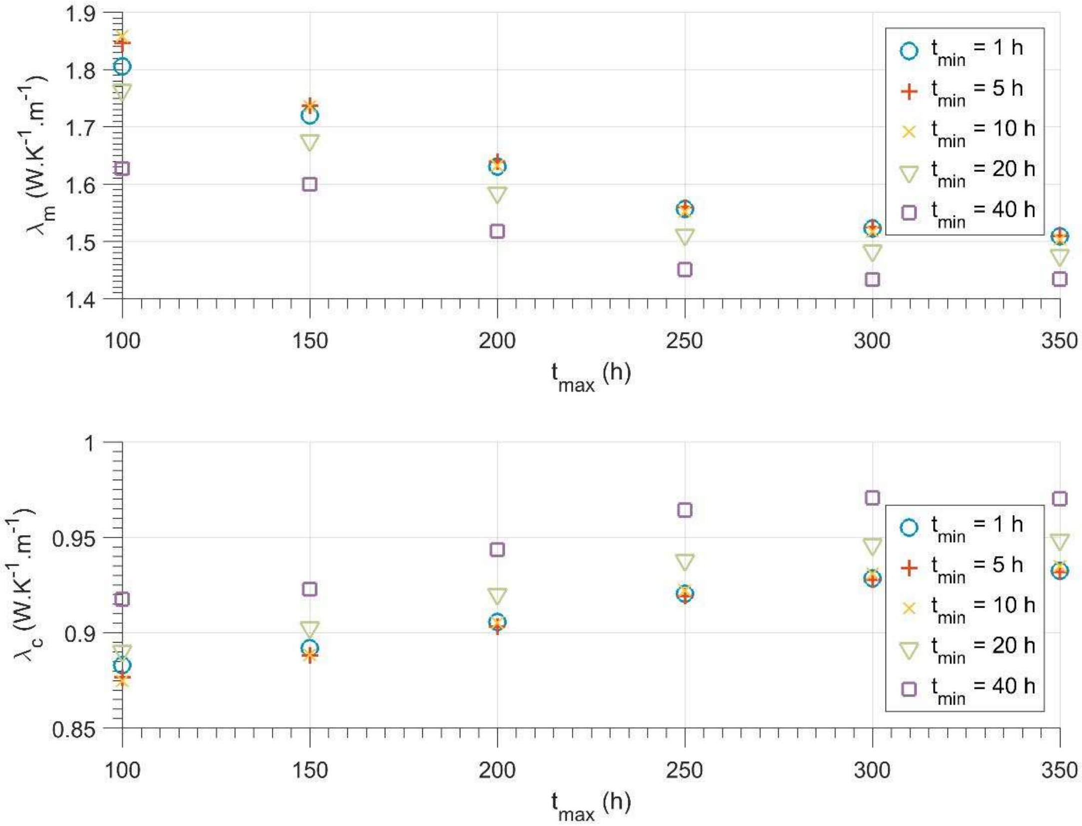

Figure 15: Interpretation with the SA model: λ_m and λ_c as a function of the integration times t_{min} and t_{max}

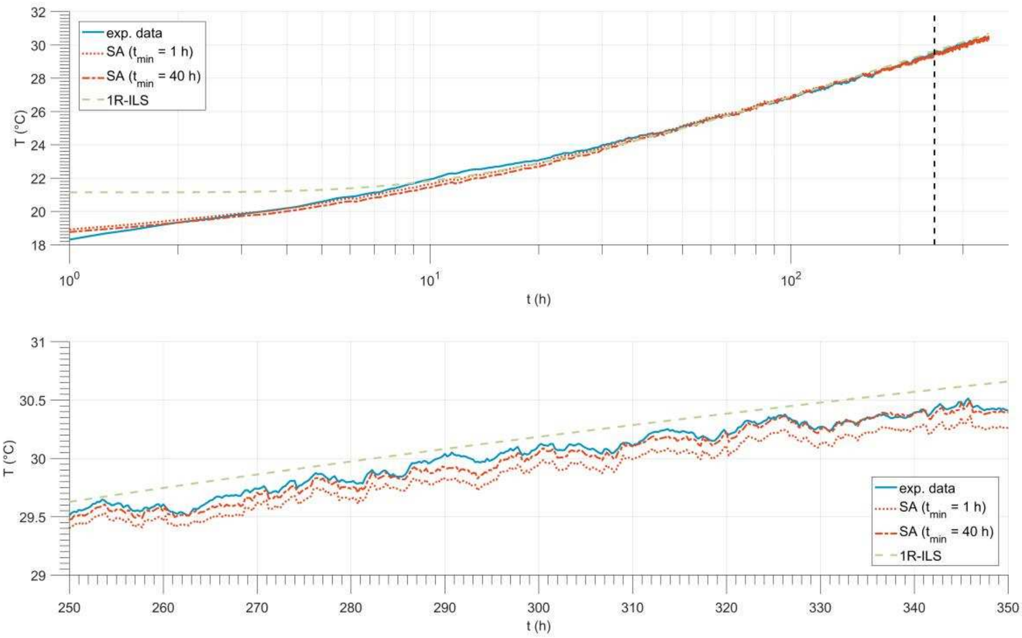

Figure 16: Evolution of the mean fluid temperature: Experimental data, SA model with $t_{min} = 1$ h, $t_{min} = 40$ h, classical model. The black-dotted vertical line accounts for $t_{max} = 250$ h, which has been used as the upper bound of integration for the three models.

5. Conclusion

A semi-analytical (SA) model to compute the temperature evolution in PHE was developed. It relies on relevant resistive-capacitive circuits accounting for PHE internal thermal inertia and hollow semi-infinite cylindrical source step-response to account for long-term vertical heat transfer around the pile. The SA model has been checked against a finite element code. Both models are in excellent agreement at a range of timescales. However further research effort is needed to better understand the thermal interactions between the pile and the above building, and how this can be dealt with in analytical G-function.

The SA model was compared to a purely resistive (1R) model that neglects thermal inertia in the PHE. The results suggest that the 1R model always overestimate the PHE outlet temperature, no matter the pipe radius and positions, or the ground and concrete thermal conductivities. In other words, the 1R model always underestimates the PHE performances. Taking into consideration thermal transfers within the PHE in dynamic simulation tools would improve the assessment of PHE performances and their potential of development.

Purely resistive models developed for Borehole Heat Exchangers (BHE) are barely suitable for the interpretation of thermal response tests (TRT) performed on PHE. Therefore, the SA model was used to analyse a TRT performed on a PHE of radius 30 cm. The main result is that for this type of large PHE, the TRT duration should be of 250 h, so that reliable values of ground and concrete thermal conductivities are determined.

The SA model has been developed for a PHE equipped with 4 pipes and for impervious ground conditions. Further developments will focus on extending the SA model to configurations with a larger number of pipes and integrating step-responses accounting for underground water flow and a group of piles.

6. Acknowledgement

The development of the semi-analytical model described in this paper is a part of a research project ‘‘GECKO’’, geo-structures and hybrid solar panel coupling for optimized energy storage, (2011-2015) which is supported by a grant from the French National Research Agency (ANR) under reference “ANR-11-SEED-0013-06”.

The exploitation of the semi-analytical model for TRT analysis was funded by the European Network for Shallow Geothermal Energy Applications in Buildings and Infrastructure COST-GABI, under reference “ECOST-STSM-TU1405-280216-071379 STSM”. The TRT data was provided by Crossrail, based on tests conducted by GI Energy. This project would not have been possible without their support.

The second author greatfully acknowledges financial support from the Royal Academy of Engineering in the UK.

7. References

[1] EurObserv'ER, Ground-source heat pump barometer, Systèmes Solaires. (2011).

[2] EurObserv'ER, Heat pumps barometer, 2015.

[3] D. Pahud, M. Hubbuch, Mesures et optimisation de l'installation avec pieux énergétiques du Dock Midfield de l'aéroport de Zürich, 2007.

[4] F. Loveridge, W. Powrie, Temperature response functions (G-functions) for single pile heat exchangers, Energy. 57 (2013) 554–564. doi:10.1016/j.energy.2013.04.060.

[5] A. Bidarmaghz, G.A. Narsilio, I.W. Johnston, S. Colls, The importance of surface air temperature fluctuations on long-term performance of vertical ground heat exchangers, Geomech. Energy Environ. 6 (2016) 35–44. doi:10.1016/j.gete.2016.02.003.

[6] C.K. Lee, H.N. Lam, A simplified model of energy pile for ground-source heat pump systems, Energy. 55 (2013) 838–845. doi:10.1016/j.energy.2013.03.077.

[7] C. Yavuzturk, A Short Time Step Response Factor Model for Vertical Ground Loop Heat Exchangers, 105 (1999) 475–485.

[8] O. Ghasemi-fare, P. Basu, Predictive assessment of heat exchange performance of geothermal piles, Renew. Energy. 86 (2016) 1178–1196. doi:10.1016/j.renene.2015.08.078.

[9] H. Park, S.-R. Lee, S. Yoon, J.-C. Choi, Evaluation of thermal response and performance of PHC energy pile: Field experiments and numerical simulation, Appl. Energy. 103 (2013) 12–24. doi:10.1016/j.apenergy.2012.10.012.

[10] B. Bezyan, S. Porkhial, A.A. Mehrizi, 3-D simulation of heat transfer rate in geothermal pile-foundation heat exchangers with spiral pipe configuration, Appl. Therm. Eng. 87 (2015) 655–668. doi:10.1016/j.applthermaleng.2015.05.051.

[11] F. Cecinato, F.A. Loveridge, In fl uences on the thermal ef fi ciency of energy piles, 82 (2015). doi:10.1016/j.energy.2015.02.001.

[12] S. Park, S. Lee, K. Oh, D. Kim, H. Choi, Engineering chart for thermal performance of cast-in-place energy pile considering thermal resistance, Appl. Therm. Eng. 130 (2018) 899–921. doi:10.1016/j.applthermaleng.2017.11.065.

[13] W. Liu, M. Xu, ScienceDirect ScienceDirect ScienceDirect 2D Axisymmetric Model Research of Helical Heat Exchanger inside 2D Axisymmetric Model Research of Helical Heat Exchanger inside Pile Foundations Pile Foundations, Procedia Eng. 205 (2017) 3503–3510. doi:10.1016/j.proeng.2017.09.914.

[14] D. Wang, L. Lu, A. Pan, ScienceDirect Investigating the Impact of Thermo-physical Property Difference between Soil and Pile on the Thermal Performance of Energy Piles, Procedia Eng. 205 (2017) 3199–3205. doi:10.1016/j.proeng.2017.10.269.

[15] Q. Zhao, B. Chen, F. Liu, Study on the thermal performance of several types of energy pile ground heat exchangers : U-shaped , W-shaped and spiral-shaped, Energy Build. 133 (2016) 335–344. doi:10.1016/j.enbuild.2016.09.055.

[16] A. Abouei, S. Porkhial, B. Bezyan, H. Lot, Energy pile foundation simulation for different con

fi gurations of ground source heat exchanger ☆, 70 (2016) 105–114. doi:10.1016/j.icheatmasstransfer.2015.12.001.

[17] C. Han, X. Bill, Feasibility of geothermal heat exchanger pile-based bridge deck snow melting system : A simulation based analysis, Renew. Energy. 101 (2017) 214–224. doi:10.1016/j.renene.2016.08.062.

[18] P. Eskilson, Thermal analysis of heat extraction boreholes, University of Lund, Sweden, 1987.

[19] L.R. Ingersoll, H.J. Plass, Theory of the ground pipe heat source for the heat pump, Heating, Pip. Air Cond. (1948).

[20] H.S. Carslaw, J.C. Jaeger, Conduction of Heat in Solids, Oxford University Press, Oxford, 1947.

[21] P. Eslami-nejad, M. Bernier, Coupling of geothermal heat pumps with thermal solar collectors using double U-tube boreholes with two independent circuits, Appl. Therm. Eng. 31 (2011) 3066–3077. doi:10.1016/j.applthermaleng.2011.05.040.

[22] Y. Man, H. Yang, N. Diao, J. Liu, Z. Fang, A new model and analytical solutions for borehole and pile ground heat exchangers, Int. J. Heat Mass Transf. 53 (2010) 2593–2601. doi:10.1016/j.ijheatmasstransfer.2010.03.001.

[23] G. Hellström, Ground Heat Storage - Thermal Analyses of Duct Storage Systems, University of Lund, Sweden, 1991.

[24] H. Zeng, N. Diao, Z. Fang, Heat transfer analysis of boreholes in vertical ground heat exchangers, 46 (2003) 4467–4481. doi:10.1016/S0017-9310(03)00270-9.

[25] C. Zhang, P. Chen, Y. Liu, S. Sun, D. Peng, An improved evaluation method for thermal performance of borehole heat exchanger, Renew. Energy. 77 (2015) 142–151. doi:10.1016/j.renene.2014.12.015.

[26] D. Bauer, W. Heidemann, H. Müller-Steinhagen, H.-J.G. Diersch, Thermal resistance and capacity models for borehole heat exchangers, Int. J. Energy Res. 35 (2011) 312–320. doi:10.1002/er.1689.

[27] I.R. Maestre, F.J. González Gallero, P. Álvarez Gómez, J.D. Mena Baladés, Performance assessment of a simplified hybrid model for a vertical ground heat exchanger, Energy Build. 66 (2013) 437–444. doi:10.1016/j.enbuild.2013.07.041.

[28] A.S. Shirazi, M. Bernier, Thermal capacity effects in borehole ground heat exchangers, Energy Build. 67 (2013) 352–364. doi:10.1016/j.enbuild.2013.08.023.

[29] a. Nguyen, P. Pasquier, An adaptive segmentation Haar wavelet method for solving thermal resistance and capacity models of ground heat exchangers, Appl. Therm. Eng. 89 (2015) 70–79. doi:10.1016/j.applthermaleng.2015.05.073.

[30] M. De Rosa, F. Ruiz-Calvo, J.M. Corberán, C. Montagud, L. a. Tagliafico, A novel TRNSYS type for short-term borehole heat exchanger simulation: B2G model, Energy Convers. Manag. 100 (2015) 347–357. doi:10.1016/j.enconman.2015.05.021.

[31] P. Eslami-Nejad, M. Bernier, Coupling of geothermal heat pumps with thermal solar collectors using double U-tube boreholes with two independent circuits, Appl. Therm. Eng.

31 (2011) 3066–3077. doi:10.1016/j.applthermaleng.2011.05.040.

[32] T. Oppelt, I. Riehl, U. Gross, Modelling of the borehole filling of double U-pipe heat exchangers, Geothermics. 39 (2010) 270–276. doi:10.1016/j.geothermics.2010.06.001.

[33] F. Loveridge, W. Powrie, G-Functions for multiple interacting pile heat exchangers, Energy. 64 (2014) 747–757. doi:10.1016/j.energy.2013.11.014.

[34] D. Bozis, K. Papakostas, N. Kyriakis, On the evaluation of design parameters effects on the heat transfer efficiency of energy piles, Energy Build. 43 (2011) 1020–1029. doi:10.1016/j.enbuild.2010.12.028.

[35] M. Li, A.C.K. Lai, New temperature response functions (G functions) for pile and borehole ground heat exchangers based on composite-medium line-source theory, Energy. 38 (2012) 255–263. doi:10.1016/j.energy.2011.12.004.

[36] W. Zhang, P. Cui, J. Liu, X. Liu, Study on heat transfer experiments and mathematical models of the energy pile of building, Energy Build. 152 (2017) 643–652. doi:10.1016/j.enbuild.2017.07.041.

[37] W. Zhang, H. Yang, P. Cui, L. Lu, N. Diao, Z. Fang, Study on spiral source models revealing groundwater transfusion effects on pile foundation ground heat exchangers, Int. J. Heat Mass Transf. 84 (2015) 119–129. doi:10.1016/j.ijheatmasstransfer.2014.12.036.

[38] G. Zhou, Y. Zhou, D. Zhang, Analytical solutions for two pile foundation heat exchanger models in a double-layered ground, Energy. 112 (2016) 655–668. doi:10.1016/j.energy.2016.06.125.

[39] D. Wang, L. Lu, P. Cui, International Journal of Heat and Mass Transfer A novel composite-medium solution for pile geothermal heat exchangers with spiral coils, Int. J. Heat Mass Transf. 93 (2016) 760–769. doi:10.1016/j.ijheatmasstransfer.2015.10.055.

[40] A. Zarrella, M. De Carli, A. Galgaro, Thermal performance of two types of energy foundation pile: Helical pipe and triple U-tube, Appl. Therm. Eng. 61 (2013) 301–310. doi:10.1016/j.applthermaleng.2013.08.011.

[41] S. Javed, J. Spitler, Accuracy of borehole thermal resistance calculation methods for grouted single U-tube ground heat exchangers, Appl. Energy. 187 (2017) 790–806. doi:10.1016/j.apenergy.2016.11.079.

[42] L. Lamarche, B. Beauchamp, A new contribution to the finite line-source model for geothermal boreholes, Energy Build. 39 (2007) 188–198. doi:10.1016/j.enbuild.2006.06.003.

[43] M. Philippe, M. Bernier, D. Marchio, Validity ranges of three analytical solutions to heat transfer in the vicinity of single boreholes, Geothermics. 38 (2009) 407–413. doi:10.1016/j.geothermics.2009.07.002.

[44] L. Lamarche, S. Kajl, B. Beauchamp, A review of methods to evaluate borehole thermal resistances in geothermal heat-pump systems, Geothermics. 39 (2010) 187–200. doi:10.1016/j.geothermics.2010.03.003.

[45] VDI-Gesellschaft Verfahrenstechnik und Chemieingenieurwesen., VDI Wärmeatlas: Wärmeübertragung bei der Strömung durch Rohre (heat transfer in flow through pipes)., 10th ed., Springer, 2006.

[46] J.a. Rivera, P. Blum, P. Bayer, Ground energy balance for borehole heat exchangers: Vertical fluxes, groundwater and storage, Renew. Energy. 83 (2015) 1341–1351. doi:10.1016/j.renene.2015.05.051.

[47] J.A. Rivera, P. Blum, P. Bayer, Influence of spatially variable ground heat flux on closed-loop geothermal systems: Line source model with nonhomogeneous Cauchy-type top boundary conditions, Appl. Energy. 180 (2016) 572–585. doi:10.1016/j.apenergy.2016.06.074.

[48] J.A. Rivera, P. Blum, P. Bayer, A fi nite line source model with Cauchy-type top boundary conditions for simulating near surface effects on borehole heat exchangers, Energy. 98 (2016) 50–63. doi:10.1016/j.energy.2015.12.129.

[49] SIA, Norme Suisse. Sondes géothermiques. SIA 384/6, Société suisse des ingénieurs et des architectes, Zurich, 2010.

[50] F. Loveridge, W. Powrie, D. Nicholson, Comparison of two different models for pile thermal response test interpretation, Acta Geotech. 9 (2014) 367–384. doi:10.1007/s11440-014-0306-3.

[51] V. Wagner, P. Blum, M. Kübert, P. Bayer, Analytical approach to groundwater-influenced thermal response tests of grouted borehole heat exchangers, Geothermics. 46 (2013) 22–31. doi:10.1016/j.geothermics.2012.10.005.

[52] S. Gehlin, Thermal Response Test - Method, Development and Evaluation [Doctoral Thesis], Luleå University of Technology, 2002.

[53] F. Loveridge, W. Powrie, Geothermics 2D thermal resistance of pile heat exchangers, Geothermics. 50 (2014) 122–135. doi:10.1016/j.geothermics.2013.09.015.

[54] J.L. Fernández-Martínez, E. García-Gonzalo, The generalized PSO: a new door to PSO evolution, J. Artif. Evol. Appl. 2008 (2008). doi:10.1155/2008/861275.

Annex A: Determination of the RC parameters

The normalized RC parameters as defined in (8) were fitted to minimize an objective function ε (see Figure A-1). ε is defined as a combination of root mean square error between the normalized energies e* computed by the RC model and e* by a FE code. ε was weighted by the asymptotic values of energy in two simulations:

$$\varepsilon = \frac{e^*_{sim\,1,\infty}\,\varepsilon_{sim\,1} + e^*_{sim\,2,\infty}\,\varepsilon_{sim\,2}}{e^*_{sim\,1,\infty} + e^*_{sim\,2,\infty}} \tag{A.1}$$

For both simulations 1 and 2 the initial temperature is zero (T* = 0). In simulation 1, T* = 1 is set on one pipe while the borehole wall and all the other pipes are maintained to the initial temperature (T* = 0). In simulation 2, T* = 1 is set on all the pipes while the borehole wall is kept at the initial temperature (T* = 0) (cf. Figure A.1).

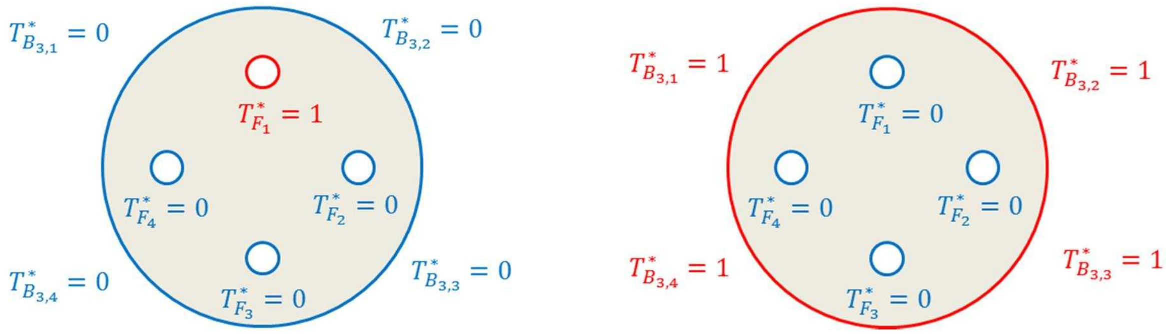

Figure A.1: Boundary condition for simulation #1 (left) and simulation #2 (right)

Solving simulation 1 in steady state leads to:

$$\begin{cases} q^*_{F_1} = -\dfrac{1}{R^*_1} - \left(1 - \dfrac{1}{4}\right)\dfrac{1}{R^*_2} - \dfrac{1}{R^*_3} \\ q^*_{F_2} = \dfrac{1}{4\,R^*_2} + \dfrac{1}{2\,R^*_1} \\ q = \dfrac{1}{4\,R^*_2} \end{cases} \Rightarrow \begin{cases} R^*_1 = \dfrac{1}{2\left(q^*_{F_2} - q^*_{F_3}\right)} \\ R^*_2 = \dfrac{1}{4\,q^*_{F_3}} \\ R^*_3 = -\dfrac{1}{q^*_{F_1} + 2q^*_{F_2} + q^*_{F_3}} \end{cases} \tag{A.2}$$

Where $p^*_{F_1}$, $p^*_{F_2}$ and $p^*_{F_3}$ refer to the power exchanged at pipes F_1, F_2 and F_3 respectively; $R_1^* = R_{2,1}^* + R_{2,2}^*$, R_2^* and $R_3^* = R_{3,1}^* + R_{3,2}^* + R_{3,3}$.

Three parameters x_2, y_2, y_3 are introduced to describe the location of $C_{B,1}$, $C_{B,2}$ and $C_{M,2}$:

$$\begin{aligned} x_2 &= \frac{R_{21}}{R_2} \\ x_3 &= \frac{R_{31}}{R_3} \\ y_3 &= \frac{R_{32}}{R_3} \end{aligned} \tag{A.3}$$

Simulation 2 focuses on testing the outer part of the RC circuit (i.e. from node F_1 to B_3) while simulation 1 tests both this outer part and the heart of the RC circuit. In simulation 2 only C_{B1}, C_{B2} and x_2 play a role. The heat balance on nodes B_1^* and B_2^* gives:

$$\begin{bmatrix} C_{B1}^* & 0 \\ 0 & C_{B2}^* \end{bmatrix} \frac{d}{dt^*} \begin{Bmatrix} T_{B1}^* \\ T_{B2}^* \end{Bmatrix} + \begin{bmatrix} \frac{1}{R_{32}^*} + \frac{1}{R_{31}^*} & -\frac{1}{R_{32}^*} \\ -\frac{1}{R_{32}^*} & \frac{1}{R_{32}^*} + \frac{1}{R_{33}^*} \end{bmatrix} \begin{Bmatrix} T_{B1}^* \\ T_{B2}^* \end{Bmatrix} = \begin{Bmatrix} 0 \\ \frac{1}{R_{33}^*} \end{Bmatrix} \tag{A.4}$$

The energy in the pile section reads:

$$e_{sim\,2}^*(t^*) = 4\left(C_{B1}^*\, T_{B1}^*(t^*) + C_{B2}^*\, T_{B2}^*(t^*)\right) \tag{A.5}$$

Noticing that in steady state the temperature at the nodes B_1 and B_2 are respectively equal to x_3 and $x_3 + y_3$, the energy in steady state reads:

$$e_{sim\,2,\infty}^* = 4\left[C_{B1}^* x_3 + C_{B2}^*(x_3 + y_3)\right] \tag{A.6}$$

For simulation 1, a heat balance leads to:

$$\begin{bmatrix} C_{B1}^* & 0 & 0 & 0 & 0 & 0 \\ 0 & C_{B2}^* & 0 & 0 & 0 & 0 \\ 0 & 0 & 0 & 0 & 0 & 0 \\ 0 & 0 & 0 & C_{M2}^* & 0 & 0 \\ 0 & 0 & 0 & 0 & C_{M2}^* & 0 \\ 0 & 0 & 0 & 0 & 0 & C_{M1}^* \end{bmatrix} \frac{d}{dt^*} \begin{Bmatrix} T_{B1}^* \\ T_{B2}^* \\ T_{A1}^* \\ T_{C1}^* \\ T_{C2}^* \\ T_M^* \end{Bmatrix}$$

$$+ \begin{bmatrix} \frac{1}{R_{31}^*} + \frac{1}{R_{32}^*} & -\frac{1}{R_{32}^*} & 0 & 0 & 0 & 0 \\ -\frac{1}{R_{32}^*} & \frac{1}{R_{32}^*} + \frac{1}{R_{33}^*} & 0 & 0 & 0 & 0 \\ 0 & 0 & \frac{2}{R_1^*} & 0 & 0 & 0 \\ 0 & 0 & 0 & \frac{1}{R_{21}^*} + \frac{1}{R_{22}^*} & 0 & -\frac{1}{R_{22}^*} \\ 0 & 0 & 0 & 0 & \frac{1}{R_{21}^*} + \frac{1}{R_{22}^*} & -\frac{1}{R_{22}^*} \\ 0 & 0 & 0 & -\frac{1}{R_{22}^*} & -\frac{n-1}{R_{22}^*} & \frac{n}{R_{22}^*} \end{bmatrix} \begin{Bmatrix} T_{B1}^* \\ T_{B2}^* \\ T_{A1}^* \\ T_{C1}^* \\ T_{C2}^* \\ T_M^* \end{Bmatrix} = \begin{Bmatrix} \frac{1}{R_{31}^*} \\ 0 \\ \frac{1}{R_1^*} \\ \frac{1}{R_{21}^*} \\ 0 \\ 0 \end{Bmatrix}$$

(A.7)

The energy in the pile section is:

$$e_{sim\,1}^*(t) = C_{B2}^*\, T_{B2}^*(t) + C_{B1}^*\, T_{B1}^*(t) + C_{M2}^*\, T_{C1}^*(t) + 3\, C_{M2}^*\, T_{C2}^*(t) + C_{M1}^*\, T_M^*(t) \tag{A.8}$$

The additivity of thermal capacities leads to the following constraint:

$$4\left(C_{B1}^* + C_{B2}^* + C_{M2}^*\right) + C_{M1}^* = \pi\left(1 - 4\, r_p^{*2}\right) \tag{A.9}$$

Equations A.4 and A.7 were solved with the ode45 function for ordinary derivative equations in MATLAB® Software. The internal time step used by the ode45 was left up to ode45, with the output with being exported at every normalized time step $\Delta t^* = 10^{-2}$ up to $t^* = 5$. $t^* = 5$ was used as it ensured the steady-state to be reached. Similarly, the inner time step used by COMSOL was left to the software, with output being exported on the same period. The reader is referred to the supporting information for further details on this numerical procedure.

The objective function ε (eq. A.1) was minimized when fulfilling equality constraints and with a Particule Swarm Optimization (PSO) algorithm [54] (cf. Figure A-1 for one confiugration).

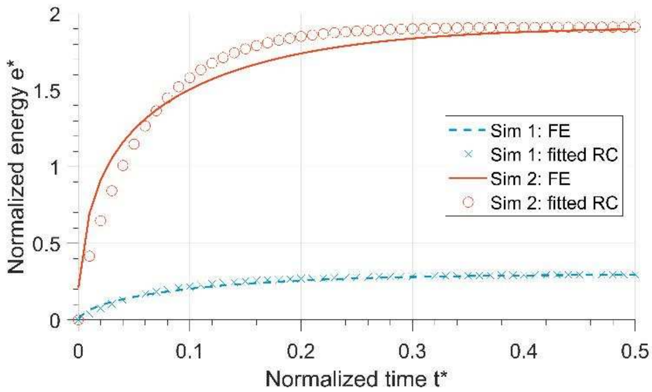

Figure A-1: Evolution of normalized energy for Sim *1* and Sim *2* from FE model and RC model with fitted parameters. Configuration defined by r_p* = 0.0533 and s* = 1.417.

The procedure is iterated over 181 configurations, each configuration being characterized by a value of r_p* and s* satisfying geometric constrains c_1, c_2, c_3 as represented in Figure 6. Capacities and capacity locations exhibit some rough behaviour, and are smoothed through a quadratic form was determined for every parameter p (capacity or location):

$$p(r_p{}^*, s^*) = a_1 + a_2 r_p{}^* + a_3 s^* + a_4 r_p{}^* s^* + a_5 r_p{}^{*2} + a_6 s^2 \quad \text{(A.10)}$$

Finally, values for the 10 RC model parameters for the 181 configurations are exported in a table, available in the supporting information of the paper.

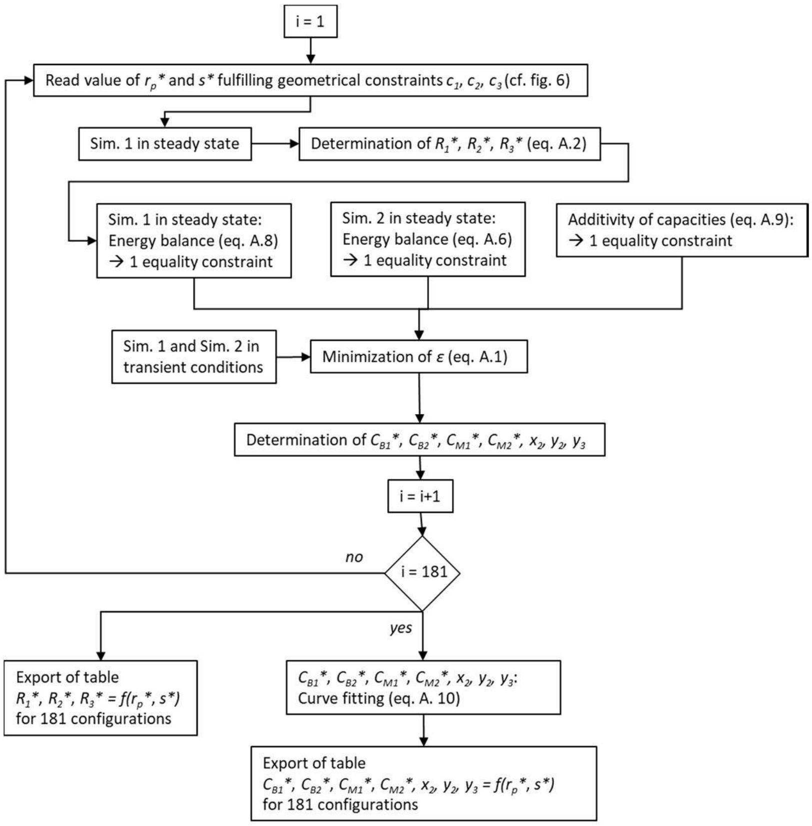

Figure A-2: Overall process for determination of the RC parameters

Annex B: Assembling matrices

Let us consider a pile with 4 pipes i (i=1,..,4) connected in serial. {T} contains the inlet temperature T_{in}, the PHE temperature and the borehole wall temperature T_p :

$$\{T\} = \begin{Bmatrix} T_{in} \\ \{T_1\}_{8\times 1} \\ \{T_2\}_{8\times 1} \\ \{T_3\}_{8\times 1} \\ \{T_4\}_{8\times 1} \\ T_M \\ T_p \end{Bmatrix} \tag{B.1}$$

$\{T_i\}_{8x1}$ contains the temperature in a pile section around a pile. The temperatures are assumed to be independent upon the depth:

$$\{T_i\}_{8\times 1} = \begin{Bmatrix} T_{A,i} \\ T_{C,i} \\ T_{fl,i} \\ T_{F,i} \\ T_{B1,i} \\ T_{B2,i} \\ p_i/\lambda_0 \\ T_{fds,i} \end{Bmatrix} \tag{B.2}$$

The conductance matrix $[\Lambda]$ is given by assembling submatrices:

$$[\Lambda] = \begin{bmatrix} [0]_{1\times 1} & [\Lambda_N]_{1\times 8} & [\Lambda_N]_{1\times 8} & [\Lambda_N]_{1\times 8} & [\Lambda_N]_{1\times 8} & [0]_{1\times 2} \\ [\Lambda_W]_{8\times 1} & [\Lambda_c]_{8\times 8} & [\Lambda_{12}]_{8\times 8} & [0]_{8\times 8} & [\Lambda_{1n}]_{8\times 8} & [\Lambda_E]_{8\times 2} \\ [0]_{8\times 1} & [\Lambda_{21}]_{8\times 8} & [\Lambda_c]_{8\times 8} & [\Lambda_{12}]_{8\times 8} & [0]_{8\times 8} & [\Lambda_E]_{8\times 2} \\ [0]_{8\times 1} & [0]_{8\times 8} & [\Lambda_{21}]_{8\times 8} & [\Lambda_c]_{8\times 8} & [\Lambda_{12}]_{8\times 8} & [\Lambda_E]_{8\times 2} \\ [0]_{8\times 1} & [\Lambda_{n1}]_{8\times 8} & [0]_{8\times 8} & [\Lambda_{21}]_{8\times 8} & [\Lambda_c]_{8\times 8} & [\Lambda_E]_{8\times 2} \\ [0]_{2\times 1} & [\Lambda_S]_{2\times 8} & [\Lambda_S]_{2\times 8} & [\Lambda_S]_{2\times 8} & [\Lambda_S]_{2\times 8} & [\Lambda_{SE}]_{2\times 2} \end{bmatrix}$$

(B.3)

The submatrices $[\Lambda_c]$, $[\Lambda_W]$, $[\Lambda_S]$, $[\Lambda_{SE}]$, $[\Lambda_E]$, $[\Lambda_N]$ $[\Lambda_{12}]$, $[\Lambda_{21}]$, $[\Lambda_{1n}]$, $[\Lambda_{n1}]$ are given by:

$$[\Lambda_c] = \begin{bmatrix} \frac{2}{R_1} & 0 & 0 & -\frac{1}{R_1} & 0 & 0 & 0 & 0 \\ 0 & \frac{1}{R_{21}}+\frac{2}{R_1} & 0 & -\frac{1}{R_1} & 0 & 0 & 0 & 0 \\ 0 & 0 & \frac{1}{R_p} & -\frac{1}{R_p} & 0 & 0 & -\lambda_0 & 0 \\ -\frac{1}{R_1} & -\frac{1}{R_{21}} & -\frac{1}{R_p} & \frac{1}{R_p}+\frac{1}{R_{21}}+\frac{2}{R_1}+\frac{1}{R_{31}} & -\frac{1}{R_{31}} & 0 & 0 & 0 \\ 0 & 0 & 0 & -\frac{1}{R_{31}} & \frac{1}{R_{31}}+\frac{1}{R_{32}} & -\frac{1}{R_{32}} & 0 & 0 \\ 0 & 0 & 0 & 0 & -\frac{1}{R_{32}} & \frac{1}{R_{32}}+-\frac{1}{R_{33}} & 0 & 0 \\ 0 & 0 & -2\lambda_0 & 0 & 0 & 0 & 0 & \lambda_0 \\ 0 & 0 & 0 & 0 & 0 & 0 & \lambda_0 & \lambda_0\frac{P^{n+1}}{H\Delta T} \end{bmatrix}$$

$$[\Lambda_N] = [0 \quad 0 \quad 0 \quad 0 \quad 0 \quad 0 \quad \lambda_0 \quad 0]$$

$$[\Lambda_W] = \begin{bmatrix} 0 \\ 0 \\ 0 \\ 0 \\ 0 \\ 0 \\ \lambda_0 \\ -\frac{P^{n+1}}{H\Delta T}\lambda_0 \end{bmatrix}$$

$$[\Lambda_S] = \begin{bmatrix} 0 & -\frac{1}{R_{22}} & 0 & 0 & 0 & 0 & 0 & 0 \\ 0 & 0 & 0 & 0 & 0 & 0 & -\frac{4G^n}{R_{33}} & 0 \end{bmatrix}$$

$$[\Lambda_E] = \begin{bmatrix} -\frac{1}{R_{22}} & 0 \\ 0 & 0 \\ 0 & 0 \\ 0 & 0 \\ 0 & 0 \\ 0 & -\frac{1}{R_{33}} \\ 0 & 0 \\ 0 & 0 \end{bmatrix}$$

$$[\Lambda_{SE}] = \begin{bmatrix} \frac{4}{R_{22}} & 0 \\ 0 & \lambda_m + \frac{4G^n}{R_{33}} \end{bmatrix}$$

$$[\Lambda_{12}] = \begin{bmatrix} 0 & 0 & 0 & -\frac{1}{R_1} & 0 & 0 & 0 & 0 \\ 0 & 0 & 0 & 0 & 0 & 0 & 0 & 0 \\ 0 & 0 & 0 & 0 & 0 & 0 & 0 & 0 \\ 0 & 0 & 0 & 0 & 0 & 0 & 0 & 0 \\ 0 & 0 & 0 & 0 & 0 & 0 & 0 & 0 \\ 0 & 0 & 0 & 0 & 0 & 0 & 0 & 0 \\ 0 & 0 & 0 & 0 & 0 & 0 & 0 & 0 \\ 0 & 0 & 0 & 0 & 0 & 0 & 0 & 0 \end{bmatrix}$$

$$[\Lambda_{21}] = \begin{bmatrix} 0 & 0 & 0 & 0 & 0 & 0 & 0 & 0 \\ 0 & 0 & 0 & 0 & 0 & 0 & 0 & 0 \\ 0 & 0 & 0 & 0 & 0 & 0 & 0 & 0 \\ -\frac{1}{R_1} & 0 & 0 & 0 & 0 & 0 & 0 & 0 \\ 0 & 0 & 0 & 0 & 0 & 0 & 0 & 0 \\ 0 & 0 & 0 & 0 & 0 & 0 & 0 & 0 \\ 0 & 0 & 0 & 0 & 0 & 0 & 0 & 1 \\ 0 & 0 & 0 & 0 & 0 & 0 & 0 & \frac{P^{n+1}}{H\Delta T} \end{bmatrix}$$

$$[\Lambda_{1n}] = \begin{bmatrix} 0 & 0 & 0 & 0 & 0 & 0 & 0 & 0 \\ 0 & 0 & 0 & 0 & 0 & 0 & 0 & 0 \\ 0 & 0 & 0 & 0 & 0 & 0 & 0 & 0 \\ -\frac{1}{R_1} & 0 & 0 & 0 & 0 & 0 & 0 & 0 \\ 0 & 0 & 0 & 0 & 0 & 0 & 0 & 0 \\ 0 & 0 & 0 & 0 & 0 & 0 & 0 & 0 \\ 0 & 0 & 0 & 0 & 0 & 0 & 0 & 0 \\ 0 & 0 & 0 & 0 & 0 & 0 & 0 & 0 \end{bmatrix}$$

$$[\Lambda_{n1}] = \begin{bmatrix} 0 & 0 & 0 & -\frac{1}{R_1} & 0 & 0 & 0 & 0 \\ 0 & 0 & 0 & 0 & 0 & 0 & 0 & 0 \\ 0 & 0 & 0 & 0 & 0 & 0 & 0 & 0 \\ 0 & 0 & 0 & 0 & 0 & 0 & 0 & 0 \\ 0 & 0 & 0 & 0 & 0 & 0 & 0 & 0 \\ 0 & 0 & 0 & 0 & 0 & 0 & 0 & 0 \\ 0 & 0 & 0 & 0 & 0 & 0 & 0 & 1 \\ 0 & 0 & 0 & 0 & 0 & 0 & 0 & 0 \end{bmatrix}$$

(B.4)

In eq. (B.4) λ_0 is a reference thermal conductivity of the same order of magnitude as λ_m (e.g. 1 W.K^{-1}.m^{-1}) introduced for unit consistency. R_p accounts for the effective thermal resistance of the pipe, including both advection within the fluid and heat conduction in the pipe material. Note that the power P is evaluated at the next time step P^{n+1}. The capacitance matrix $[\mathcal{C}]$ reads:

$$[\mathcal{C}] = \begin{bmatrix} [0]_{1\times 1} & [0]_{1\times 8} & [0]_{1\times 8} & [0]_{1\times 8} & [0]_{1\times 8} & [0]_{1\times 2} \\ [0]_{8\times 1} & [\mathcal{C}_0]_{8\times 8} & [0]_{8\times 8} & [0]_{8\times 8} & [0]_{8\times 8} & [0]_{8\times 2} \\ [0]_{8\times 1} & [0]_{8\times 8} & [\mathcal{C}_0]_{8\times 8} & [0]_{8\times 8} & [0]_{8\times 8} & [0]_{8\times 2} \\ [0]_{8\times 1} & [0]_{8\times 8} & [0]_{8\times 8} & [\mathcal{C}_0]_{8\times 8} & [0]_{8\times 8} & [0]_{8\times 2} \\ [0]_{8\times 1} & [0]_{8\times 8} & [0]_{2\times 8} & [0]_{8\times 8} & [\mathcal{C}_0]_{8\times 8} & [0]_{8\times 2} \\ [0]_{2\times 1} & [0]_{2\times 8} & [0]_{2\times 8} & [0]_{2\times 8} & [0]_{2\times 8} & [0]_{2\times 2} \end{bmatrix} \quad \text{(B.5)}$$

With:

$$[\mathcal{C}_0]_{8\times 8} = \begin{bmatrix} 0 & 0 & 0 & 0 & 0 & 0 & 0 & 0 \\ 0 & \mathcal{C}_{M2} & 0 & 0 & 0 & 0 & 0 & 0 \\ 0 & 0 & 0 & 0 & 0 & 0 & 0 & 0 \\ 0 & 0 & 0 & 0 & 0 & 0 & 0 & 0 \\ 0 & 0 & 0 & 0 & \mathcal{C}_{B1} & 0 & 0 & 0 \\ 0 & 0 & 0 & 0 & 0 & \mathcal{C}_{B2} & 0 & 0 \\ 0 & 0 & 0 & 0 & 0 & 0 & 0 & 0 \\ 0 & 0 & 0 & 0 & 0 & 0 & 0 & 0 \end{bmatrix} \tag{B.6}$$

And the right member $[\wp]$ reads:

$$\{\wp\} = \left\{ \begin{array}{c} \dfrac{P^{n+1}}{H} \\ [0]_{(35)\times 1} \\ \left\{ \begin{array}{c} 0 \text{ if } n = 1 \\ \lambda_m T_0 + \left(p_b{}^1(G^2 - G^1)\right) \text{ if } n = 2 \\ \lambda_m T_0 + \left(p_b{}^1 G^n + \displaystyle\sum_{l=1}^{n-2} \left(p_b{}^{l+1} - p_b{}^{l}\right) G^{n-l} - p_b{}^{n-1} G^1\right) \text{ if } n > 2 \end{array} \right. \end{array} \right\} \tag{B.7}$$